Fluid-Structure-Electrophysiology interaction (FSEI) in the left–heart: a multi-way coupled computational model.

Francesco Viola[a,*], Valentina Meschini[b], Roberto Verzicco[c,a,b]

[a] *PoF group, University of Twente, The Netherlands*
[b] *Gran Sasso Science Institute, Italy*
[c] *Department of Industrial Engineering, University of Roma Tor Vergata, Italy*

Abstract

In this study we present a computational model for unprecedented simulations of the left heart in realistic physiological conditions. To this aim, models for the electrical network of contractile muscular fibers (electrophysiology bidomain model), the myocardium mechanics (shells with hyperelastic and orthotropic constitutive relations) and the complex hemodynamics (direct numerical simulation of the Navier–Stokes equations) have been developed and multi–way coupled. The resulting multi–physics model, relying on the immersed–boundary method to cope with the complex fluid–structure interaction, is then validated by replicating the dynamics of the left heart considering simultaneously its atrium and ventricle, with the embedded aortic and mitral valves, and the thoracic aorta where blood is pumped. It is shown that the developed model, when given as input the parameters for the human heart, can reproduce the physiologic velocity and pressure signals obtained by cardiographic diagnostics of real patients.

Keywords: Cardiovascular flows, Hemodynamics, Multiphysics model, Computational engineering

*Corresponding author
Email address: f.viola@utwente.nl (Francesco Viola)

1. Introduction

Every day the human heart beats approximately 10^5 times to ensure the delivery of oxygen and nutrients to all body cells and the removal of their waste products. Each beat is triggered by specialized pacemaker cells that generate rhythmical electrical impulses rapidly propagating through the heart, stimulating myocytes contraction and, in turn, pumping blood. The resulting hemodynamics yields shear stresses and pressure loads on the myocardium and on the valve leaflets, whose opening/closing ensures the correct flow direction across heart chambers. Only the synchronized and synergistic action of the electrophysiology, mechanics of the myocardium and hemodynamics allows the heart of an adult human to pump 5 l/min of blood to the whole body using a power of only 8 W, lifelong (indeed out of a total power of 8W about only 2W go directly to the fluid while the rest produces heat which is anyway beneficial to keep constant the internal body temperature).

Unfortunately, because of the perfect and highly sophisticated mechanism, even a minor malfunctioning affects the whole heart and reduces its pumping efficiency thus impairing all the body. For this reason cardiovascular disorders (CVD) are the main cause of death in developed countries [1, 2] and also one of the most relevant costs for health care systems [3]. In order to counter the alarming CVD cost projections for the next decades novel approaches, capable of improving the currently available tools without increasing their costs, are needed and computational engineering can be very effective for this purpose.

In fact, computer simulations of the blood flow in the heart and arteries can be a precious tool to improve the predicting capabilities of diagnostics, to refine surgical techniques and test the performance of prosthetic devices. Computational methods allow the evaluation of quantities that would be exceedingly difficult or impossible to measure *in vivo* or *in vitro* and they permit the virtual testing of innovative technologies without relying entirely on experiments. On the other hand, the reliability of cardiovascular simulations depends on the accurate modeling of the hemodynamics, the realistic characterization of the

tissues and the correct description of the fluid/structure interaction [4]. Unfortunately simulating the whole heart with this level of detail is a formidable task that should be tackled by successive steps and, with this goal in mind, we have decided to start from the left heart.

Simulating the left heart (LH) is not just halving the complexity of the problem since its modelling requires the solution of all the difficulties of the whole organ. In fact, a realistic description of the LH has to consider the physiology of the myocardium made of fibers that contract actively and are activated by an electrical signal whose propagation can only be described by the full electrophysiology. This model, in turn, must be connected with the hemodynamics in complex geometry heart chambers and valves and their tissue mechanics which are coupled through fluid/structure interaction (FSI). We wish to stress that, besides being a significant step towards the modelling of the whole heart, simulating its left part has also important practical and clinical implications since it is the most subjected to cardiovascular disorders having to withstand the highest pressure differences [5].

In the literature there is plenty of studies in which the full problem has been reduced by using simplifying assumptions, by dealing with single parts of the LH or more complex functional units. For example, [6, 7] have considered the FSI problem for the flow in a deformable aorta predicting data of clinical interest such as shear stress, tissue deformations, pressure waveforms and flow velocities. When also the dynamics of the aortic valve has been considered, the problem has been simplified by integrating only part of the cycle [8], imposing symmetries [9] or resorting to a rigid aortic root [10, 11] so as to decrease the computational cost. In some cases, turbulence models have been used to avoid the explicit simulation of the smallest flow scales [12, 13] thus reducing substantially the nodes of the computational mesh and allowing for larger integration time steps. More recently, the full three–dimensional flow through a mechanical and biologic prosthetic aortic valve in an elastic aortic root has been investigated [14, 15, 16], showing the clinical implications of the altered vortex dynamics produced by the prostheses.

Some more recent studies have focussed on the left ventricular flow in presence of natural and prosthetic mitral valves. In particular, the effectiveness of the ventricle wash–out has been studied as function of the ventricle pumping efficiency [17], mitral valve geometry and possible presence of stenoses [17, 18]. In these papers the full FSI between hemodynamics and deformable tissues was considered even if the contraction and relaxation of the ventricle was driven by an externally imposed flow rate rather than being determined by the active contraction of the myocardium. In some cases the problem complexity has been further reduced by prescribing the time–dependent tissue deformations through model analytical functions or using patient–specific kinematics [19] obtained by medical imaging. In this case, however, the effect of the flow on the myocardium contraction and expansion is disregarded and the blood motion can only adapt to the imposed wall displacement thus loosing all the coupled dynamics.

In order to simulate in detail the heart dynamics, the active contraction and relaxation of the tissues has to be modeled by including its electrophysiology and the muscle activation. Several accurate models are available from the literature [20, 21, 22, 23] capable of predicting the time dependent propagation of the electrical signal over the cardiac tissue and the local contractile tension generated by the activated myocytes. The electromechanical models and their numerical solution are nowadays well–assessed tools [24, 25, 26] and they have been employed to dissect the mechanisms for cardiac dysfunctions. However, the fluid dynamic part is generally neglected or its effect simply modeled prescribing a time–dependent pressure acting on the endocardium, thus missing the rich cardiac hemodynamics and the shear stresses (WSS) originated at the wall. Only few attempts have been made to couple the hemodynamics with electrophysiology [27, 28] although the mesh for the flow was too coarse to fully resolve the flow, therefore compromising the physiologic realism of the results. On the other hand, accurate flow solution in a left ventricle and aortic root was obtained in [29] but resorting to a simplified lumped–parameter model for the cardiac tissue and artificially imposing the action potential to trigger the left ventricle contraction. Another important limitation was that the electrophys-

iology and the fluid–structure computations were performed separately, thus missing the full electrical–fluid–structure coupling. This implies that the coupling was only one–way and that the feedback of the blood loads on the tissues was neglected.

It appears that, although strongly coupled in reality, so far the electrophysiology– and the FSI–models have remained segregated in most of the studies, presumably owing to the bottleneck of available accurate and efficient solvers for the Navier–Stokes equations.

The present work aims at bridging this gap by fully coupling the electrophysiology and the FSI into an integrated computational model for the flow in an 'animated' LH with realistic geometry and electrophysiology. This will allow to reproduce, by high fidelity simulations, physiological heart conditions without prescribing any motion to the heart tissues whose kinematics will be instead part of the model solution. In particular, being valve leaflets and aorta passive structures, their motion will be determined by the hydrodynamic loads and internal tissues stresses only. In contrast, ventricle and atrium are active tissues therefore their dynamics will include the muscular contraction.

Hence, to properly model the LH three different physical models and their full coupling will be exploited. The resulting electro–fluid–structure interaction (FSEI) model will be then employed to study the physiological hemodynamics in the LH, which pumps oxygenated blood through the systemic circulation providing with oxygenated blood most of the organs and tissues of the body.

2. Problem description and numerical methods

We consider the set–up for the human LH, shown in figure 1, made of two chambers, left atrium and ventricle, which are separated by the mitral valve. Although our computational model can cope with realistic geometries, including those coming from an ECO or CT of a specific patient, the present geometry is not patient specific and it has been built from high-resolution clinical images and medical atlas [30] using modeling software. The left atrium receives

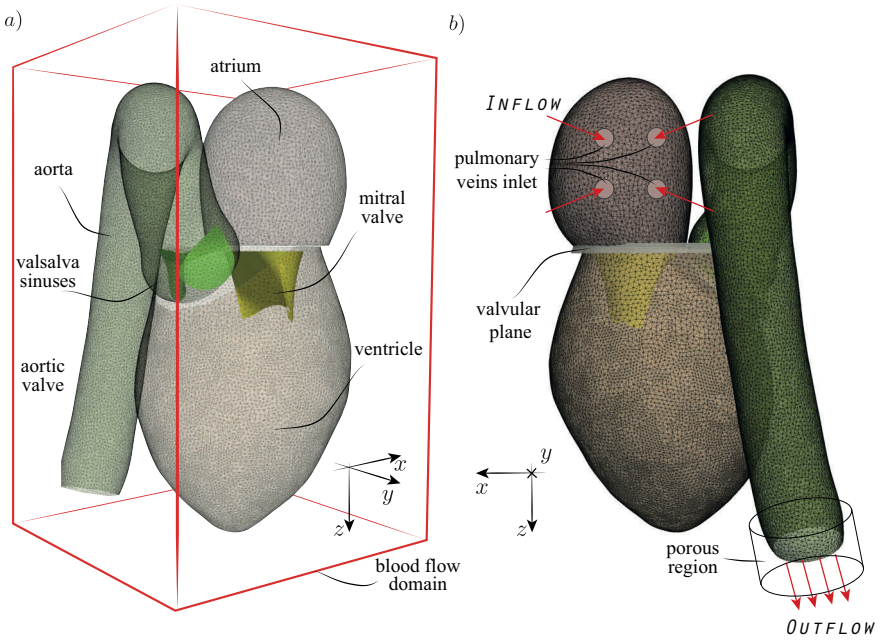


Figure 1: (a) Front and (b) rear visualization of the numerical set-up for left heart simulations. The red-box in (a) indicates the computational domain for the fluid solver.

oxygenated blood from the lungs via the inlet in the pulmonary veins, and is connected to the left ventricle through the mitral valve that has two leaflets, one (anterior) next to the aortic valve and the other (posterior) close to the lateral myocardium. The left ventricle pumps blood through the aorta causing the aortic valve to open during systole and to close during diastole. The aortic valve is made of three cusps placed just before the Valsalva sinuses, which are the three bulges of the aortic root originating from the left ventricle (see figure 1a). The ascending aorta bends 180° down in the aortic arch and then extends in the thoracic descending aorta. These eight moving and deformable bodies are then anchored to the valvular plane (the fibrous trine), which is stiffer with respect to the other heart tissues and is here modeled as a rigid body. The valvular plane has two circular orifices of diameter $d^m = 24$ mm and $d^a = 19$ mm where the mitral and aortic valves are mounted. The mitral leaflets are modeled as deformable membranes 2 mm thick and placed inside a deformable left ventri-

cle of thickness 8 mm with short and long axes equal to 58 mm and 75 mm respectively, and a stress–free volume of 125 ml. The three aortic leaflets are 1.5 mm thick and connected to the thoracic aorta with a wall thickness of 3 mm and diameter ranging from 40 mm at the root, 30 mm at the arch and about 22 mm in the descending part. The atrium is 4 mm thick with a stress–free volume of 40 ml, and the pulmonary veins ostia have a diameter of 10 mm. The reference frame is defined with the z-axis oriented as the longer ventricle axis and pointing down towards its apex. Hence, the $x - y$ plane is parallel to the mitral orifice. The whole LH is immersed into a rectangular domain of size $l_x \times l_y \times l_z = 95 \times 95 \times 140$ mm^3 and indicated by the red box in figure 1(a), where the Navier–Stokes equations are solved. As typical in the IBM [31, 17], a computational domain larger than the one of interest is discretized by structured Cartesian mesh and the no–slip condition on all the tissues is enforced through a body force in the Navier–Stokes equations as detailed in the next section. Henceforth, the fluid domain outside the domain of interest (the left heart in this case) has not direct physical meaning and it only serves for computational support.

In reality, the LH is just one part of the whole circulatory system therefore boundary conditions must be imposed at the inlets and outlet of the model in order to represent the vascular network not included in the computational domain. In this model, blood enters the atrium through the pulmonary vein inlets and leaves the system through the thoracic aorta (figure 1b). Although the pulmonary veins are not discretized, the LH model accounts for their inlet at the posterior atrial wall as visible in figure 1b. Specifically, the atrial wall has four orefices (corresponding to the pulmonary veins inlets), which connect the atrium to the outer bulk of the computational domain (in which the left heart is immersed) and the blood can freely move from the outer bulk through the pulmonary veins inlet thus feeding the atrium during early diastole. However, during the A–wave, the atrial contraction would generate an unrealistic backflow that, *in-vivo* is prevented by the lungs impedance setting an upstream pressure level and a favorable pressure gradient towards the atrium. Since the

lungs are not included in our computational model, during atrial contraction (lasting about 10% of the cycle) the undesired back flow has been prevented by artificially closing the vein inlets using body forces defined by the IBM. Hence, the inflow at the pulmonary veins inlet (corresponding to the intel of the left heart) is not prescribed and the incoming mass flow rate is a result of the simulation itself. It will be shown that this simple modelling of the pulmonary veins, along with the use of an accurate electrophysiological model, ensures the correct pressure values in the heart chambers. Similarly, the impedance of the missing systemic circulation has been parametrized at the end of the thoracic aorta by a fixed porous volume indicated in figure 1b, whereas the compliance contribution is provided by the elastic aortic tissue. Specifically, in the outflow region an artificial Darcy's force of the type $\mathrm{k}^{-1}\mathbf{u}$ is added at the right-hand-side of the Navier-Stokes equations (1) where the permeability $\mathrm{k} = 0.001$, which sets the after load of the system, is chosen after a parametric study in such a way to allow within a heart cycle the same flow rate as the one pumped by the left ventricle. As we will see later, this allows the aorta to attain a periodic dynamics in which it neither empties nor fills up over the heartbeats. We remark that the porous region corresponding to the outlet of the left heart is placed inside the computational domain and not at its lower boundary, where a no-slip condition on the velocity is imposed (see section 2.1).

The simulations are always initiated at systole, when the aortic and mitral valves are closed, and ventricle and atrium are in the tele-diastolic configuration. Hence, at $t = 0$ valve leaflets and heart chambers are in the stress-free configuration, except for the aorta, which is pretensioned by an external force providing a ground pressure of 60 mmHg in the aortic root. It is worth mentioning that being the dynamics periodic in time, any phase of the cycle could be used as initial condition; the beginning of the systole is, however, the most convenient because only the aorta needs a pretensioning load.

We turn now to describe the 'building blocks' needed to realize the multi–physics model and their integration. In the next three subsections the governing equations for the hemodynamics, structural dynamics and electrophysiology

along with their numerical discretization are introduced and discussed while in the last subsection all the run parameters and convergence checks are given.

2.1. Fluid mechanics

The blood velocity, $\mathbf{u}$, and pressure p, are governed by the Navier–Stokes and continuity equations, which in non–dimensional form read:

$$\begin{aligned} \frac{\partial \mathbf{u}}{\partial t} + \mathbf{u} \cdot \nabla \mathbf{u} &= -\nabla p + \nabla \cdot \boldsymbol{\tau} + \mathbf{f}, \\ \nabla \cdot \mathbf{u} &= 0. \end{aligned} \tag{1}$$

In the case of a Newtonian fluid, the viscous stress tensor $\boldsymbol{\tau}$ is given by $Re^{-1}(\nabla \mathbf{u} + \nabla^T \mathbf{u})$, whereas non–Newtonian fluids call for more complex constitutive relations. Blood is a concentrated suspension of cells, mainly erythrocytes, in a Newtonian liquid, the plasma, therefore its overall behavior is that of a non–Newtonian fluid owing to the surface tension of the cell membranes on the Newtonian matrix. In order to account also for this behaviour a non–Newtonian (shear–thinning, Carreau–Yasuda) blood model has been implemented in the flow solver [32] even if it has been shown that the non–Newtonian blood features become relevant only in vessels of sub–millimeter diameter [33] while in the ventricular flow they produce only minor effects [17]. Accordingly, in the present study we have used the Newtonian fluid model with an effective kinematic viscosity of $\nu = 4.8 \times 10^{-6}$ m^{2}s^{-1} which is that for human blood with an hematocrit of 40% [34, 35]. The Reynolds number is defined as $Re = U^m d^m/\nu$ being $d^m = 2.4$ cm the mitral annulus diameter and $U^m = 60$ cm/s the average velocity through the mitral annulus during diastole, which is typically measured using Doppler echocardiography [36]: the resulting Reynolds number is $Re = U^m d^m/\nu = 3000$.

The governing equations (1) are solved using the Navier–Stokes solver AFiD [37, 38], which is based on central second–order finite–differences discretized on a staggered mesh and it has been already extensively tested in previous studies for a variety of flow configurations: additional details of the numerical scheme can be found in [39, 40, 38]. The code is equipped with several immersed bound-

ary (IB) techniques to solve the fluid dynamics around moving and deformable objects. Indeed, the forcing term $\mathbf{f}$ in equation (1) is the IB volume forcing incorporated in the fluid solver to impose the no–slip boundary condition on the velocity at the fluid/structure interfaces. For the purpose of discussion of the general concepts, let us consider $\hat{\mathbf{u}}$ the intermediate solution that satisfies the time-discretized momentum equation:

$$\frac{\hat{\mathbf{u}} - \mathbf{u}^n}{\Delta t} = -\alpha_1 \nabla p^n + \gamma_1 H^n + \rho_1 H^{n-1} + \frac{\alpha_1}{2Re} \nabla^2 (\hat{\mathbf{u}} + \mathbf{u}^n), \tag{2}$$

where $\mathbf{u}^n$ denotes the velocity at time t^n, Δt is the time step, H gathers the nonlinear terms and the coefficient of the time advancement scheme are equal to $\gamma_1 = 3/2$, $\rho_1 = -1/2$ and $\alpha_1 = \gamma_1 + \rho_1 = 1$ [31]. In order to ensure a sufficient resolution of the immersed surface and avoid unphysical mass fluxes through it, the no-slip boundary condition has to be enforced on some Lagrangian markers uniformly distributed on the IB, with a spacing comparable to the local Eulerian grid. Given $\mathbf{V}_b$ the local velocity of a Lagrangian marker laying on the the body at position $\mathbf{x}_b$, the i-component of the forcing that sets the local velocity of the fluid, $\mathbf{u}(\mathbf{x}_b)$, equal to $\mathbf{V}_b$ (no-slip condition) is then simply

$$F_i(\mathbf{x}_b) = \frac{V_{bi} - u_i^n(\mathbf{x}_b)}{\Delta t}, \tag{3}$$

where V_{bi} and $u_i^n(\mathbf{x}_b)$ are the i-components of $\mathbf{V}_b$ and $\mathbf{u}^n(\mathbf{x}_b)$, respectively. This expressions for the direct IB forcing is formally valid in the case that the Lagrangian marker position, $\mathbf{x}_b$, coincides with an Eulerian grid–point for the fluid, which is in general not the case, especially for moving and deformable bodies. In particular, since equations (2) are discretized using staggered finite differences, the marker can not be simultaneously coincident to each staggered grid used for the three velocity components and, therefore, an interpolation procedure for the forcing (3) is needed.

The presence of the valvular plane, which is here modeled as a fixed rigid body, is represented by the IB technique proposed by [41] where the no-slip condition at the body surface is translated, through a linear interpolation, to a condition on the first grid point external to the body, $\mathbf{x}_1$. As shown in figure 2(a),

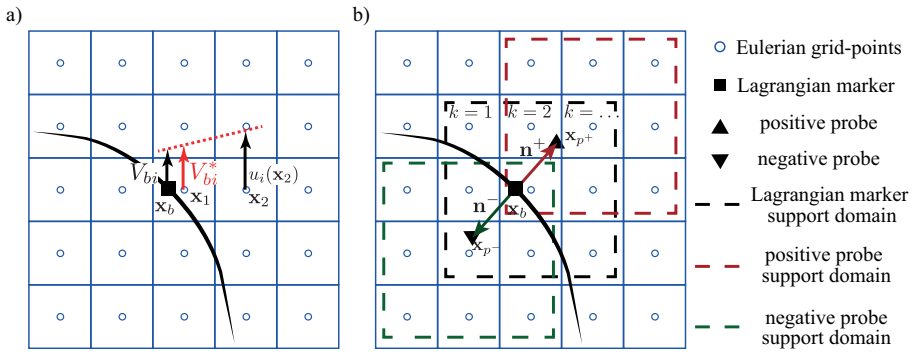


Figure 2: Two-dimensional sketch of the IB forces evaluation for (a) rigid and (b) deformable bodies.

the i–component of the velocity at $\mathbf{x}_1$, V^*_{bi}, is obtained by linearly interpolating the velocity at the second grid point $u_i(\mathbf{x}_2)$ (that is known by the Navier–Stokes solution at time t^n) and the velocity at the body surface V_{bi}. Hence, the IB forcing (3) applied at the body position $\mathbf{x}_b$ converts into the following forcing

$$F_i(\mathbf{x}_1) = \frac{V^*_{bi} - u^n(\mathbf{x}_1)}{\Delta t}, \tag{4}$$

acting at the first grid point external to the body. Although this method preserves the second-order accuracy of the finite-difference scheme [41], the corresponding hydrodynamic stresses are only first-order accurate with the error scaling as the local distance between the body position and the first external grid point $||\mathbf{x}_1 - \mathbf{x}_b||$. The latter quantity varies both in space (according to the body shape) and in time (for moving bodies) thus yielding strong oscillations of the hydrodynamical forces due to insufficient numerical accuracy. In the case of rigid bodies, where their motion only depends on the net hydrodynamic loads, the random error on the local stress smooths out in the integration over the body surface and the FSI coupling is correctly solved [11]. In contrast, in the case of deformable bodies, an inaccuracy on the local stress would lead to a spurious local deformation of the tissue that, in turn, may originate an unphysical hydrodynamic load resulting in a subsequent incorrect tissue configuration.

In order to overcome this numerical instability mechanism arising by the di-

rect formulation (4), a moving-least-square (MLS) approach for the IB forcing similar to that proposed by [42] is adopted for the heart chambers, valve leaflets and aorta. Following the idea of [43], the forcing (3) is computed on the Lagrangian markers laying on the immersed surface and then transferred to several Eulerian grid-points, rather than to a single grid-point as done for rigid bodies (see equation 4). Given a Lagrangian marker a three–dimensional support domain around it consisting of $N_e = 3 \times 3 \times 3 = 27$ Eulerian nodes is created, as sketched in figure 2(b) for a two dimensional support domain consisting of nine Eulerian cells around the marker. The fluid velocity at the body position $\mathbf{u}^n(\mathbf{x}_b)$ is computed interpolating the velocity of the N_e Eulerian grid-points in the support domain as

$$u_i(\mathbf{x}_b) = \sum_{k=1}^{N_e} \phi_i^k(\mathbf{x}_b) u_i(\mathbf{x}_k), \tag{5}$$

where the $\phi_i^k(\mathbf{x})$ are the transfer operators that depend on the shape functions used for the interpolation. In this work, we consider the linear basis function $\mathbf{p}^T(\mathbf{x}) = [1, x, y, z]$ that is cost-efficient and also able to represent the gradients in the Eulerian field with second order accuracy. Since the size of the basis $\mathbf{p}$ is smaller than the number of grid-points in the support domain ($N_e > 4$), the weight operators $\phi_i^k(\mathbf{x})$ are determined so as to minimize the weighted least-square error according to the MLS method, as detailed in [31, 44]. The interpolated velocity (5) is used compute the IB force at the exact location of the marker according to equation (3), which is then transferred back to the Eulerian grid-points as a distributed forcing

$$f_i^k(\mathbf{x}_k) = \varsigma \phi_i^k(\mathbf{x}_b) F_i(\mathbf{x}_b) \qquad \text{for } k = 1 \dots N_e, \tag{6}$$

where $f_i^k(\mathbf{x}_k)$ is the i-component of the distributed IB forcing applied at the k-th grid-point of the support domain. The scaling factor ς is obtained imposing that the total forcing acting on the fluid is not changed by the transfer

$$\sum_{k=1}^{N_e} f_i^k \Delta V^k = F_i \Delta V \qquad \Rightarrow \qquad \varsigma = \frac{\Delta V}{\sum_{k=1}^{N_e} \phi^k \Delta V^k}, \tag{7}$$

where ΔV^k is the forcing volume associated with each Eulerian point (equal to the Eulerian cell volume) and $\Delta V = Ah$ is the forcing volume associated with the Lagrangian marker, with A the area of the corresponding mesh triangle and h the average mesh size at the marker location, $h = 1/3 \sum_{k=1}^{N_e} \phi_i^k (\Delta x^k + \Delta^k + \Delta z^k)$. This procedure is repeated over all Lagrangian markers for the three velocity components and the resulting IB forcing is applied to update the intermediate velocity $\hat{\mathbf{u}}$ as

$$\frac{\mathbf{u}^* - \hat{\mathbf{u}}}{\Delta t} = \mathbf{f} \qquad \Rightarrow \qquad \mathbf{u}^* = \hat{\mathbf{u}} + \Delta t \mathbf{f}. \tag{8}$$

Hence, the provisional non–solenoidal velocity $\mathbf{u}^*$, which satisfies the momentum equation (2) and respects the no–slip condition over the immersed bodies, is then projected into a divergence-free space by applying the pressure correction

$$\frac{\mathbf{u}^{n+1} - \mathbf{u}^*}{\Delta t} = \alpha_1 \nabla \Phi \qquad \Rightarrow \qquad \mathbf{u}^{n+1} = \mathbf{u}^* - \alpha_1 \Delta t \nabla \Phi. \tag{9}$$

The scalar field Φ is solution of $\nabla^2 \Phi = \nabla \cdot \mathbf{u}^* / (\alpha_1 \Delta t)$ and the pressure at time t^{n+1} reads

$$p^{n+1} = p^n + \Phi - \frac{\alpha_1 \Delta t}{2Re} \nabla^2 \Phi, \tag{10}$$

where the last two terms at the right-hand-side of equation (10) account for the solenoidal velocity correction in the unsteady and viscous term in the discrete momentum equation (2).

The hydrodynamic forces used to evolve the tissue mechanics (see section 2.4) are calculated by considering the pressure and viscous stresses at the Lagrangian markers laying on the immersed body surface. For closed surfaces, such as the ventricle, aorta and atrium, where the hydrodynamic loads only act on the inner surface, the local force contribution on a surface element of area A_j and space orientation $\mathbf{n}_j$ is given by:

$$\mathbf{F}_j^{ext} = [-p\mathbf{n}_j + \boldsymbol{\tau} \cdot \mathbf{n}_j] A_j, \tag{11}$$

(no summation is implied over the repeated indices). On the other hand, for the valve leaflets that are wet on both side by the blood, one has to account for

the forces due to the presence of the fluid along the positive $\mathbf{n}^+$ and negative $\mathbf{n}^- = -\mathbf{n}^+$ normal directions

$$\mathbf{F}_j^{ext} = [-(p^+ - p^-)\mathbf{n}_j^+ + (\tau^+ - \tau^-) \cdot \mathbf{n}_j^+]A_j. \tag{12}$$

In order to evaluate the local hydrodynamic loads (11,12), for each Lagrangian marker a probe is created along its normal direction at a distance h, equal to the averaged local grid size and, using the same MLS formulation described above, pressure and velocity derivatives are evaluated at the probe location $\mathbf{x}_p$:

$$p(\mathbf{x}_p) = \sum_{k=1}^{N_e} \phi_p^k(\mathbf{x}_p) p(\mathbf{x}_k), \qquad \left.\frac{\partial u_i}{\partial x_j}\right|_{\mathbf{x}=\mathbf{x}_p} = \sum_{k=1}^{N_e} \left.\frac{\partial \phi_i^k}{\partial x_j}\right|_{\mathbf{x}=\mathbf{x}_p} u_i(\mathbf{x}_k). \tag{13}$$

It has to be remarked that, since the derivatives $\partial\phi_i^k/\partial x_j$ can be computed analytically, the velocity gradient components are regular and second–order accurate. Using the boundary layer approximation, the pressure on the Lagrangian marker can be computed from the fluid pressure through

$$p(\mathbf{x}_b) = p(\mathbf{x}_p) + h\frac{D\mathbf{V}_b}{Dt} \cdot \mathbf{n}. \tag{14}$$

On the other hand, the velocity gradient on the body surface is considered equal to the one evaluated at the probes, see equation (13), and it turns out to be a good approximation provided that the grid is sufficiently refined near the body [31]. The second–order accuracy of the discretization scheme is preserved provided that the velocity of the fluid near the surface of the tissue varies linearly.

The left heart is discretized by 10^5 triangles (see figure 1a) and immersed in a fluid domain that is periodic in the x and y directions, while no-slip boundary conditions are imposed at the top and bottom boundaries. The Eulerian Cartesian meshes for the fluid are evenly distributed in the three dimensions and range from $129^2 \times 145$ up to $257^2 \times 290$ nodes. An important note here is that as the Eulerian grid for the fluid mechanics is refined, the Lagrangian resolution has to be increased in order to ensure the correct enforcement of the no-slip boundary condition on the bodies. This problem is tackled by using an adaptive Lagrangian mesh refinement procedure where the initial triangular

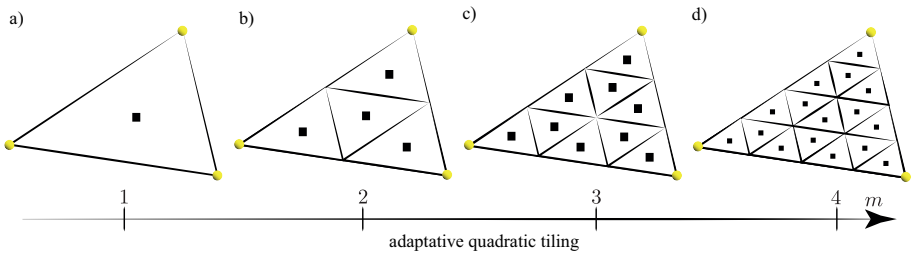


Figure 3: Adaptive quadratic tiling over an arbitrary triangle: (a) original triangle, (b) 4-tiling, (c) 9-tiling and (d) 16-tiling. The yellow circles are the vertices of a surface triangular element and the black square indicate the corresponding Lagrangian markers used to enforce the IB forcing.

mesh is automatically refined until it gets smaller than the local Eulerian grid size, thus avoiding 'holes' in the interfacial boundary condition. This approach adopted by [45], is here implemented by using a different refinement strategy based on the quadratic tailing rule for triangles [46]. An N-tiling of a triangle consists of dividing its surface in N triangles overlapping only at their boundaries whose union is congruent to the initial triangle. The quadratic tiling is a general tiling procedure to split a triangle in $N = m^2$ tiles with $m = 1, 2, 3 \ldots$ (see Figure 3) and has the property that all the tiles are similar to the original triangle. Therefore, the heart tissues are discretized independently of the Eulerian mesh and each triangle is successively refined achieving a spacing of the tiled Lagrangian grid of about 0.7 the Eulerian one. The tiling procedure can be run both, once forever at the beginning of the simulation (as done here) or dynamically at each time step according to the instantaneous tissue deformation that change the local ratio between Lagrangian and Eulerian grids. The advantage of an adaptive refinement of the Lagrangian triangulation for high Reynolds number flows is twofold: on one hand it allows the use of the same base mesh independently of the Eulerian grid and, on the other, the number of Lagrangian nodes used to deform the immersed body can be reduced. These grid resolutions along with the adaptive tiling of the triangulated tissues are seen to provide numerical convergence as it will be discussed in section 4.

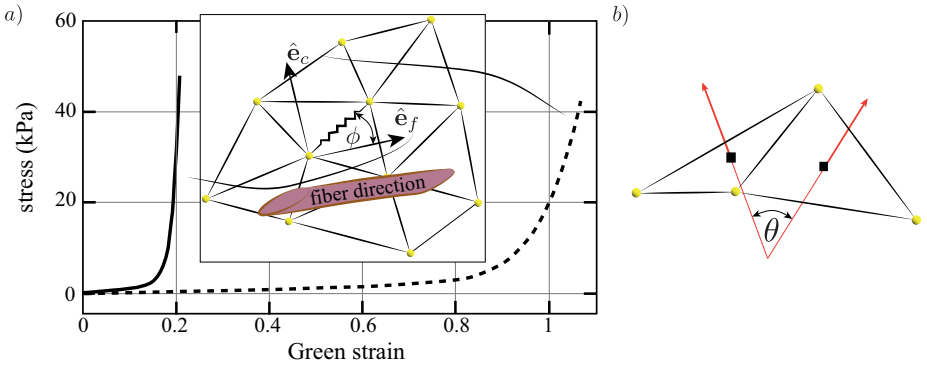


Figure 4: (a) Hyperelastic and orthotropic constitutive relation for the in-plane stiffness of the cardiac tissues. The solid and dashed lines are the stress-strain curves in the fiber ($\hat{\mathbf{e}}_f$) and cross-fiber directions ($\hat{\mathbf{e}}_c$). The inset shows the surface of any immersed body that is discretized using triangular element, whose edges are composed of non-linear springs with a certain orientation ϕ with respect to the local fiber direction. (b) The bending stiffness of the material is provided by the out-of-plane springs connecting the centroids of two adjacent triangular faces sharing an edge and inclined by an angle θ.

2.2. Structural mechanics

The structural solver is based on the Fedosov's interaction potential approach [47, 31, 48]. Any wet surface of the left heart is modeled as a thin elastic shell and is discretized by triangular meshes. The total mass of the body is lumped at its nodes proportionally to the area of the triangles sharing a given node. More precisely, given a tissue of density ρ and thickness s, the mass of the j–th triangle with surface A_j (equal to $\rho_j s_j A_j$) is equally distributed among its three nodes. Hence, the mass of the i–th node, m_i, is equal to

$$m_i = \frac{1}{3} \sum_{j=1}^{N_i} \rho_j s_j A_j, \tag{15}$$

being the summation extended only to the N_i triangles sharing the selected node i. Here, the tissue density ρ is assumed to be uniform in the LH and equal to $\rho = 1.05$ g/ml.

As shown in the inset of figure 4(a), adjacent nodes sharing an edge are connected by ideal elastic springs oriented as the mesh edges. These springs give

back an in-plane force as a response to an in-plane stretching. Additionally, the bending stiffness is provided by ideal torsional springs placed among two adjacent faces sharing an edge, and the relative rotation of two adjacent triangles stores elastic potential energy, see figure 4(b). When hydrodynamics loads and active muscular stresses are applied to the spring network, the latter deforms, thus generating internal elastic forces that are applied to the mesh nodes.

Although these elastic potentials are typically modeled in the framework of linear elastic materials [49, 31], biological cardiac tissues are strongly nonlinear and anisotropic, thus requiring a more complex constitutive relation. The anisotropy results from the fact that the heart muscle consists of fibers, and the resulting tissue is stiffer in the direction of the fibers than in the cross–fibre direction. At a given point of the tissue, therefore, we define a set of perpendicular unit vectors $\hat{\mathbf{e}}_f$-$\hat{\mathbf{e}}_c$ as in figure 4(a). To simulate the response of an hyperelastic and orthotropic material, a Fung–type constitutive relation [50, 31] is adopted, and the strain energy density reads:

$$W_e = \frac{c}{2}(e^Q - 1) \tag{16}$$

where e is Napier's constant and c is measured in Pa and Q is a combination of the Green strain tensor components [50] in the fiber, ϵ_{ff}, and cross–fiber, ϵ_{cc}, directions: $Q = \alpha_f \epsilon_{ff}^2 + \alpha_c \epsilon_{cc}^2$, with α_{ff} and α_{cc} nondimensional parameters [31]. The general expression for Q [50, 31], which includes also the cross terms of the Green strain tensor, has been simplified here under the assumption that the two stress–strain curves corresponding to equibiaxial loading (one curve for the fiber direction $\hat{\mathbf{e}}_f$ and one for the cross–fiber direction $\hat{\mathbf{e}}_c$, see figure 4a) sufficiently describe the in–plane response. Consequently, the non–null second Piola–Kirchhoff stress tensor components are $\tau_{ff} = c\alpha_{ff} e^{\alpha_{ff}\epsilon_{ff}^2}\epsilon_{ff}$ and $\tau_{cc} = c\alpha_{cc} e^{\alpha_{cc}\epsilon_{cc}^2}\epsilon_{cc}$, which correspond to the stress in the fiber and cross–fiber direction, respectively. In general, mesh edges and, consequently, in–plane springs are neither aligned nor orthogonal to the material fibers but have a generic orientation angle, ϕ, with the local fiber direction. Hence, the local in–plane stress is computed as

$$\tau_\phi = c\alpha_\phi e^{\alpha_\phi \epsilon_\phi^2}\epsilon_\phi, \tag{17}$$

where $\alpha_\phi = \sqrt{\alpha_{ff}^2 \cos^2\phi + \alpha_{cc}^2 \sin^2\phi}$ and the strain ϵ_ϕ is calculated as the spring elongation relative to its instantaneous length, i.e. $\epsilon_\phi = (l - l_0)/l$, being l and l_0, the actual and the stress–free length of the edge, respectively. Hence, given an edge of length l connecting the nodes i and j within a tissue of thickness of s, the stress (17) corresponds to the nonlinear spring forces applied to its nodes

$$\mathbf{F}_i^{el} = \tau_\phi \quad \underbrace{s\frac{A_1 + A_2}{l}}_{\text{tissue cross–section}} \quad \frac{\mathbf{r}_i - \mathbf{r}_j}{l}, \qquad \mathbf{F}_j^{el} = -\mathbf{F}_i^{el}, \tag{18}$$

with $\mathbf{r}_i$ ($\mathbf{r}_j$) the position of the node i (j) and $A_{1,2}$ the area of the triangles sharing the edge. Note that the underbraced term multiplying the stress corresponds to the tissue cross–section with respect the edge as in [49]. The parameters of the Fung constitutive relation are set as to reproduce the stress-strain curves in the fiber and cross-fiber direction measured in the ex-vivo experiments of [51, 52] for the ventricular myocardium, of [53, 54] for the aorta, of [55] for the aortic valve leaflets, of [56, 57] for the mitral valve leaflets and of [58, 59] for the atrium. In this work we have set $\alpha_{ff} = 49.56$, $\alpha_{cc} = 5.29$ and the coefficient c is equal to 13.3 Pa for the ventricle, 11.3 Pa for the aorta, 9.7 Pa for the aortic and mitral leaflets, and 12.1 Pa for the atrium. It has to be remarked that as the heart beats, its components deform significantly (e.g. ventricle volume gets about three times smaller at systole) and, consequently, the triangular mesh may get highly deformed. However, the hyperelastic material properties prevent highly skewed triangles since, as a mesh edge get deformed, the elastic force increases exponentially with the strain (see equation 17), thus regularizing the surface mesh.

The out–of–plane deformation of two adjacent triangles sharing an edge is then modeled by means of a bending spring, and the corresponding energy involves four adjacent nodes as shown in figure 4(b). Considering a surface with non–zero reference curvature in the stress–free configuration, the discretized bending energy can be written as [60]

$$W_b = k_b[1 - \cos(\theta - \theta_0)], \tag{19}$$

where θ is the angle between the normals of adjacent triangular faces of the tessellated surface, and θ_0 is the equilibrium angle determined by the spontaneous curvature, that is the shell curvature at the initial stress–free state. The bending constant is equal to $k_b = 2B/\sqrt{3}$ [61, 31], with $B = c\alpha_\phi s^3/[12(1-\nu_m^2)]$ the bending modulus of a planar structure, where s is the tissue thickness, $c\alpha_\phi$ is the equivalent Young modulus in the limit of small strain (that depend on the Fung properties of the tissues) and $\nu_m = 0.5$ is the Poisson ratio of the material. The corresponding bending nodal forces, $\mathbf{F}_j^{be}$ can be then obtained by taking the gradient of the bending potential (19) as detailed in [31]. The passive internal forces of the material at a given j–th node thus read

$$\mathbf{F}_j^{int} = \mathbf{F}_j^{el} + \mathbf{F}_j^{be}. \tag{20}$$

The structural model has also to account for the contact among different deformable tissues. In fact, during the heart beat mitral and aortic valves open and close alternatively and their leaflets are pushed against each other, during the closing phase, to seal the valve. For this purpose a contact model has been developed [18] to account for the leaflet coaptation along arbitrary surfaces in space which are *a-priori* unknown. Specifically, at each time step, the cells of the fluidic domain (red box in figure 1a) occupied by a structural node are labeled by an integer corresponding to the (arbitrary) bodies numbering, whereas untagged cells are entirely occupied by the fluid. Whenever a node of a moving body enters a tagged cell, a contact is detected and the appropriate kinematic/dynamic condition is applied. In this study we have imposed that if two nodes belonging to different bodies move to the same cell, their velocity becomes equal to their average; this prevents the structures from piercing each other during the approaching phase and allows them to freely recede if the local forces pull them apart [48]. An important advantage of this model is that two surfaces in contact can still drift together in space and they are not stuck at the initial contact position [18].

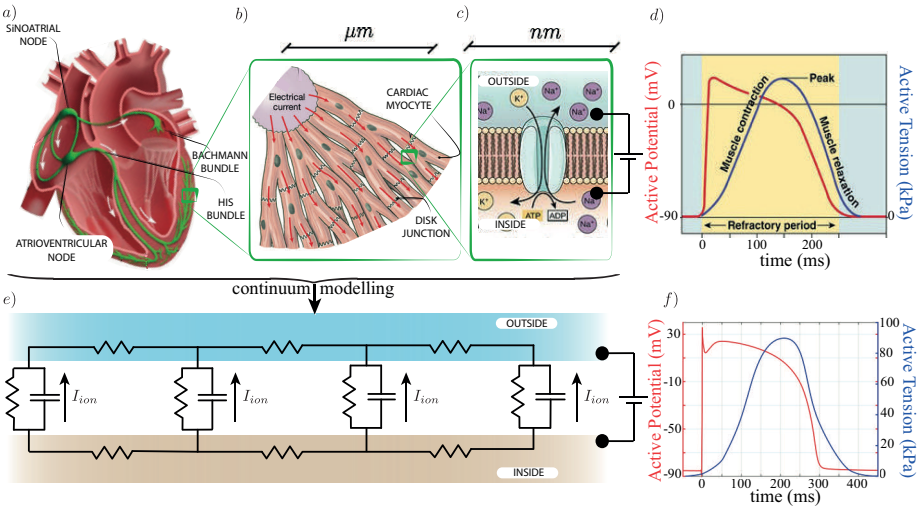


Figure 5: Electrophysiology of the heart. (a) The electrical system activates the contraction of the muscle, which is organized in (b) fibers made of myocytes. At (c) the myocytes membrane the coordinated opening/closing of ionic channels sets the transmembrane potential which varies as in (d) when cardiac cell is reached by an electrical stimulus. The depolarization/polarization cycle (action potential) triggers myocytes contraction and provides a muscular active tension (blue line). (e) The intracellular (inside) and extracellular (outside) matrices are modeled as two continuum conductive media. The solution of this bidomain model reproduces the active potential curve as shown in (f) for a representative ventricle myocyte.

2.3. Electrophysiology

Ventricles and atria are muscular chambers that contract and relax with a very precise timings in order to pump blood. The cardiac muscle is made of cardiomyocytes that are excitable cells reacting to an electrical stimulus with a mechanical contraction. These cells are organized into long fibers, see figure 5(b), and connected via disk junctions that allow ions or small molecules to pass directly from one cell to another, so that an electrical signal may propagate through adjacent cells. Specifically, when the cells are at rest, a negative potential difference v across the cell membrane (*transmembrane potential*) of about -90 mV takes place. When the cell is excited by an electrical stimulus, ionic channels at the membrane (see figure 5c) open and close in a coordinated

manner and lead the transmembrane potential to raise from its resting negative value to positive values of about $10 - 20$ mV. This phenomenon, called *cell depolarization*, is very fast (10 ms) and is followed by a relatively long repolarization process lasting about 200–300 ms (figure 5d). The complete cycle of depolarization and repolarization, called *action potential*, triggers cardiomyocytes contraction. Furthermore, the action potential triggers the activation of the surrounding cells, therefore a localized electric stimulus can propagate through the muscle and activate the complete heart.

Due to the large number of muscle cells, these complex biological processes are typically modeled using a continuum approach as sketched in figure 5(e). The cardiac tissue is modeled as an intracellular and an extracellular overlapping continuum media (*bidomain* model) separated by the cell membrane, which acts as an electrical insulator [20, 21]. The status of each domain is given by its electrical potential whose gradient gives the electric field from which the current densities are computed. Considering the conservation of charges, and the absence of external current sources, the transmembrane current is given by the gradient of the current density, which depends on the potential difference across the membrane (transmembrane potential) and on its permeability to the ions. The resulting set of partial differential equations reads

$$\begin{aligned} \chi\left(C_m\frac{\partial v}{\partial t} + I_{ion} + I_s\right) &= \nabla\cdot(M_{int}\nabla v) + \nabla\cdot(M_{int}\nabla v_{ext}), \\ 0 &= \nabla\cdot(M_{int}\nabla v + (M_{int}+M_{ext})\nabla v_{ext})), \end{aligned} \tag{21}$$

where v and v_{ext} are the transmembrane and extracellular potential (expressed in mV) to be determined. The surface–to–volume ratio of cells, χ, and the specific membrane capacitance C_m are set as in [26] equal to $\chi = 1400$ cm^{-1} $C_m = 1\mu$F cm^{-2}, respectively. The parameters M_{int} and M_{ext} are the conductivity tensors of the intracellular and extracellular media, which reflect the orthotropic myocardium electrical properties and depend on the local fiber orientation since the propagation velocity is faster along the muscle fiber than in the cross–fibers directions. According to the physiologic myocardium model by [62], here the fibers are assumed to spiral counter–clockwise in the ventricle from

the apex to the basis with a constant angle of 45° while in the atrium fibers are aligned with its vertical axis. Expressed in the basis formed by the fiber and cross-fiber directions (see figure (4)a) the local conductivity tensors M^*_{ext}, M^*_{int} are diagonal [63]

$$M^*_{ext} = \begin{bmatrix} m_{ext,f} & 0 \\ 0 & m_{ext,c} \end{bmatrix}, \qquad M^*_{int} = \begin{bmatrix} m_{int,f} & 0 \\ 0 & m_{int,c} \end{bmatrix}, \tag{22}$$

where the non-null diagonal components are the principal conductivities. Although these quantities vary throughout the myocardium [5] and the electrophysiology solver is designed to accounts for their spatial distribution, the principal conductivities have been here considered as homogeneous over the LH chambers and set as: $m_{ext,f} = 25.0$ mS/cm, $m_{ext,c} = 9.5$ mS/cm, $m_{int,f} = 7.0$ mS/cm and $m_{int,c} = 0.8$ mS/cm. The quantity I_{ion} in equation (21) is the ionic current per unit cell membrane (measured in mAcm^{-2}) that is prescribed by the cellular model. In this work two different cell models are adopted, namely the Ten Tusscher–Panfilov model [64] for the ventricle myocytes and FitzHugh–Nagumo model [65] for the atrium. Lastly, I_s is a prescribed input current to initiate the electrical propagation. In the real heart this current is generated by specialized self–oscillatory cells (*pacemaker cells*) within the sinoatrial node that is placed in the upper part of the right atrium. The electrical signal generated by the sinoatrial node then propagates towards the left ventricle and atrium passing through the His and Bachmann bundles and it is delayed by about 100 ms in the atrioventricular node (see figure 5a). In our model, however, only the left side of the heart is considered and, therefore, the electrical signal must be started differently. Specifically, a localized input current, I_s, is prescribed with the appropriate delays at the Bachmann and His bundles, respectively, for the left atrium and ventricle: these 'sparks' trigger the muscle contraction and the subsequent left heart beating in the computational model. The transmembrane potential propagation and the consequent myocardium depolarization is seen to be rather insensitive on the time duration and amplitude of I_s, and have been set to 2 ms and 35 mAcm^{-2} respectively. Instead, the time period between

two consecutive input current at the Bachmann and His bundles determines the beating period of the heart. In this work, we consider a heart beating at 70 beats-per-minute (bpm) that corresponds to a period of $T^* = 857.1$ ms (and to $T = 21.43$ nondimensional time units being $d^m/U^m = 40$ ms the characteristic time, see section 2.1). Consequently, the Womerseley number is equal to $Wo = d^m/\sqrt{T^*\nu} = 11.83$.

The set of equations 21 are discretized on the same triangular mesh as the structural solver by using the FEM libraries FEniCS [66, 67] and cbcbeat [68], which provide an efficient framework to solve for electrophysiology models over arbitrary computational domains. To determine the instantaneous muscular tension τ_{act} as a function of the transmembrane potential we adopt the evolution equation proposed by Nash and Panfilov [69]

$$\frac{\partial \tau_{act}}{\partial t} = \psi(v)[k_\tau v - \tau_{act}], \tag{23}$$

where k_τ controls the amplitude of the active stress and $\psi(v)$ is a smoothed step function (that increases monotonically from 0.1, during muscular contraction, to 1, during relaxation), which sets the delay of the active stress with respect to the action potential, see [70] for more details. The active tension τ_{act} in a tissue of local thickness s_j translates in an internal nodal active force oriented as the local muscular fiber direction:

$$\mathbf{F}_j^{act} = \tau_{act} s_j \tilde{l}_j \hat{\mathbf{e}}_f, \tag{24}$$

where $\tilde{l}_j$ is the average length of the edges sharing the j–th node.

Before concluding this section we wish to point out that, assuming the anisotropy of the intracellular and extracellular domains be the same and their conductivity tensors proportional through a scalar constant, the above bidomain model can be reduced to the *monodomain* model which requires the simulation of only a single potential field. Although both approaches are known to give very similar results for healthy tissues [21, 71] in this study we have implemented the full bidomain model in order to retain the possibility to study also pathologic configurations in the future.

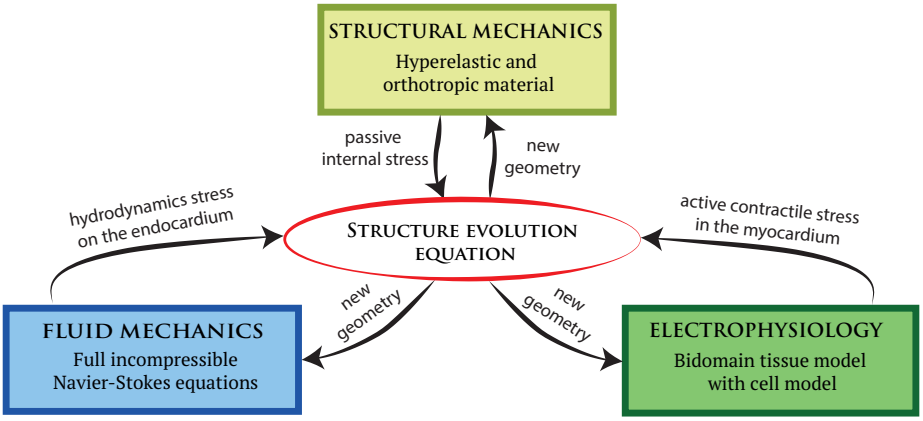


Figure 6: Sketch of the fluid–structure–electrophysiology (FSEI) coupling.

2.4. Electro–Fluid–Structure coupling

The contraction and relaxation of the heart chambers along with the aorta and valve leaflets kinematics come from the dynamic balance between inertia, external (11), passive (20) and active (24) forces acting on each triangular vertex. For each node of mass m_j (that is proportional to the local thickness, see equation 15) the second Newton law of motion applies

$$m_j \frac{\mathrm{d}^2 \mathbf{x}_j}{\mathrm{d}t^2} = \mathbf{F}_j^{ext} + \mathbf{F}_j^{int} + \mathbf{F}_j^{act}, \tag{25}$$

where $\mathbf{x}_j$ is the (instantaneous) node position and the active force is non–null only for the nodes within ventricle or atrium.

Equation (25) is integrated twice in time to determine the instantaneous tissue configuration at each time step. The new geometry can then be used as input for the fluid and electrophysiology to integrate the corresponding governing equations to obtain the new active and external forces acting, in turn, on the tissues. Owing to the strongly interconnected dynamics of the three models it is not obvious whether they must be solved simultaneously or sequentially and, in the latter case, which one has to be integrated first. In the first approach all the models are solved together as a single large dynamical system through an iterative procedure (strong coupling), while in the second the output of each model is used as input for the next one (loose coupling) in a given order. The

strong coupling is stable and robust although it is computationally demanding since it requires iterations among the solvers [31]. In contrast, the loose coupling is considerably faster but it can easily become unstable especially when added mass phenomena or structures with reduced inertia play an important role and for this reason it limits the integration time step.

In the present LH model, either the strong– and the loose–coupling procedures have been implemented and extensively tested on preliminary cases. The first approach is based on a predictor–corrector two–step Adams–Bashforth scheme and the three solvers are iterated (typically 2–4 times) until the maximum relative error computed on the position and velocity of the structural nodes drops below a prescribed threshold (usually 10^{-4}). In the loose–coupling fluid and electrophysiology are solved first and the generated hydrodynamic and active loads are used to evolve the structure whose updated configuration is the input for the successive time step.

Which of the two approaches is more efficient depends on the specific problem and its parameters; for the simulation of the LH it appears that the time step size is physically limited by the elastic frequency of the stiffer tissue, the ventricle myocardium, rather than by the stability features of the integration scheme. As a consequence, with the time–step limitations given by the ventricle dynamics, a loose coupling approach maintains the integration stable and yields the same results as the strong coupling method while providing computational time savings of the order of 50–70%, hence for all the production runs we have always used the loose–coupling. For the time integration, a dynamic time step formula provides a constant Courant number CFL = 0.2 with a maximum time step of 10^{-5} in nondimensional units that corresponds to $0.4\mu s$, which is set by the structural solver that is the most stringent for numerical stability of the FSEI method. Indeed, owing to the hyperelastic nature of the biologic tissues, the material stiffness increases steeply as the bodies are stretched or compressed, thus increasing the natural frequencies of the structure and calling for a smaller time step. Conversely, the electrophysiology manifests larger characteristic time scales that are correctly solved by the small time step used. Since in this work

we consider a heart beating at 70 beats-per-minute (bpm) with a beating period of $T = 857.1$ ms, more than 2 million time steps for each solver (fluid, structure and electrophysiology) are necessary to accurately integrate a single heart beat, with a computational cost of about 1500 CPU hours. The integration is performed over 11 heart beats for the basic grid 1 (see section 4) and, by monitoring the expansion/contraction kinematics of the left ventricle walls, a quasi–periodic regime is attained after the first cycle. As a consequence, phase–averaged quantities are computed using the last 10 heart beats (thus discarding the first one).

3. Results and discussions

We now turn to present the results of the multi-physics model in terms of electrophysiology, structure deformations and hemodynamics comparing with in-vivo and ex-vivo data. A careful grid independence analysis of the results is then shown in section 4.

3.1. Electrical activation and muscle contraction

Figure 7 shows the electrical activation and induced mechanical contraction of the LH at several instants within a heart beat. Initially, all the cells are relaxed with a negative transmembrane potential difference of about -90 mV. At a given initial time the electrical signal, here originated at the Bachmann bundle, propagates in the atrial muscle causing the cells to locally change the transmembrane conductive properties. As a consequence a rapid flux of positive ions through the cell membrane occurs, and the transmembrane potential raises to positive values, as visible from the v–isocontours reported in figure 7(a). This local depolarization results in a propagating wavefront that travels quickly across the tissue, thus activating the whole atrium and triggering the contraction of the muscle (see figure 7b). The atrial depolarization corresponds to the P wave in the electrocardiogram (ECG) signal (figure 10), and it occurs before the ventricular activation in order to allow for the complete filling of the ventricle

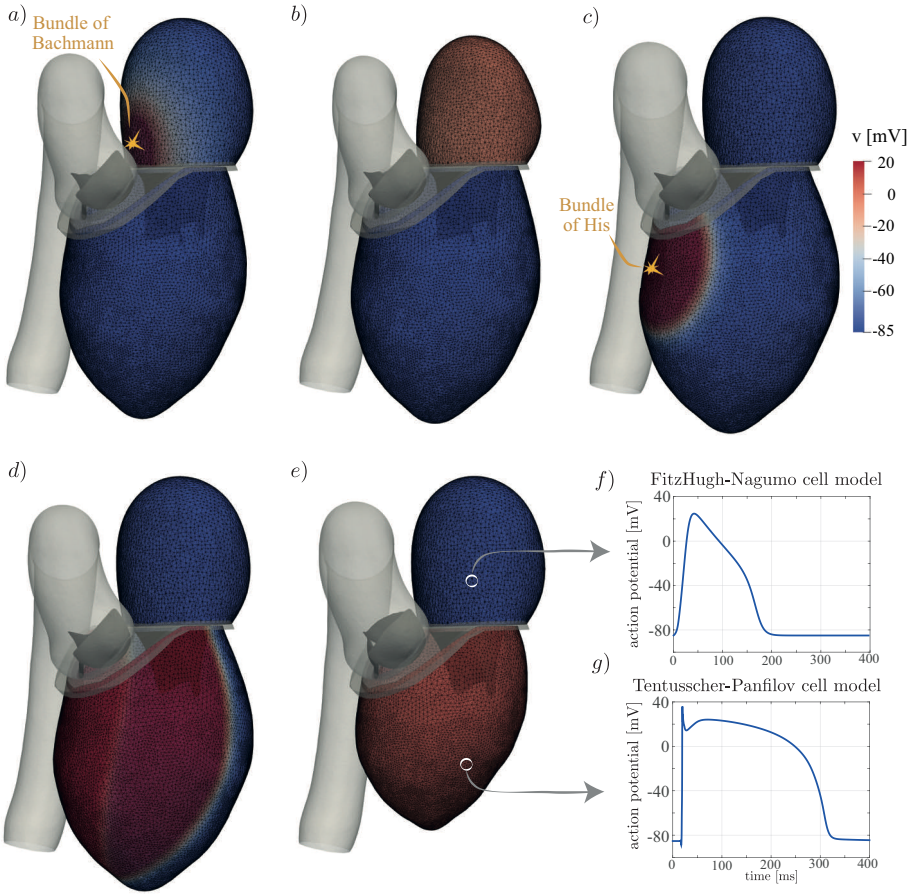


Figure 7: Snapshots of the transmembrane potential propagation in the left heart during (a) early atrial systole, corresponding to the time $t/T = 0.85$ in figure 12; (b) peak atrial systole $t/T = 0.95$; (c) early ventricular systole $t/T = 0.005$; (d) rapid propagation in the ventricular myocardium $t/T = 0.02$; (e) peak ventricular systole $t/T = 0.23$. The orange symbol in (a) and (c) depicts the Bachmann and His bundles location, where an initial stimulus current I_s is provided. The corresponding action potential curves for atrium and ventricle are shown in (f) and (g) respectively.

before starting its systole. The corresponding active potential of a typical atrial cell is reported in figure 7(f): the initial depolarization occurs in about 40 ms and it is followed by a short plateau and an immediate repolarization phase [30]. These action potential features of the atrial tissue have been accounted

for by using the appropriate cellular model (FitzHugh–Nagumo) as explained in section 2.3.

After the depolarization of the atria, the electrical signal converges to the atrioventricular node where the lower propagation speed produces a delay of about 100 ms before the ventricle activation can start. Here, an electrical stimulus, localized at the bundle of His, is applied in the form of an external electrical current I_s (equation 21) to initiate the potential propagation in the ventricle, as visible in figure 7(c). The fast propagation in the ventricular myocardium (see figure 7d) allows all portions of the ventricle to activate within a small time intervall thus inducing a strong contraction (see figure 7e) and an efficient blood pumping. The fast ventricle depolarization, corresponding to the so–called QRS–complex in the ECG (see figure 10), is followed by a fairly long plateau phase and a slow cell repolarization. During this last phase, the transmembrane potential recovers its negative resting state (corresponding to the T wave in the ECG) and the muscle relaxes. The complete ventricular myocyte cycle is shown in figure 7(g) and it is recovered by the Tentusscher–Panfilov cellular model in the equations of section 2.3.

It is worth mentioning that, since the active muscular tension follows the fibers orientation in the myocardium, according to equation (24), the model reproduces also the vigorous three–dimensional twist of the cavities from the apex to the valvular plane as observed in–vivo [62]. Figure 8 shows as during muscle contraction (panels a-c) the myocardium produces a counter–clockwise twisting, when seen from below, during systole and relaxes back by a clockwise rotation during diastole (figure 8d). This helical contraction of the ventricle ensures a swirling recirculation during systole and it is implied to assure the emptying of the endocardium trabeculae [5] thus avoiding hemostasis. Figure 9(a) reports the differential twist angle between the apex and the basis of the ventricle with a maximum twist of about 17°at the end–systole and a subsequent slow untwisting during diastole. The ventricle torsion resulting from the numerics (red line) agrees well with in-vivo measurements (black line) that have been obtained by averaging the data reported in [72, 73, 74, 75] with the error bars corresponding

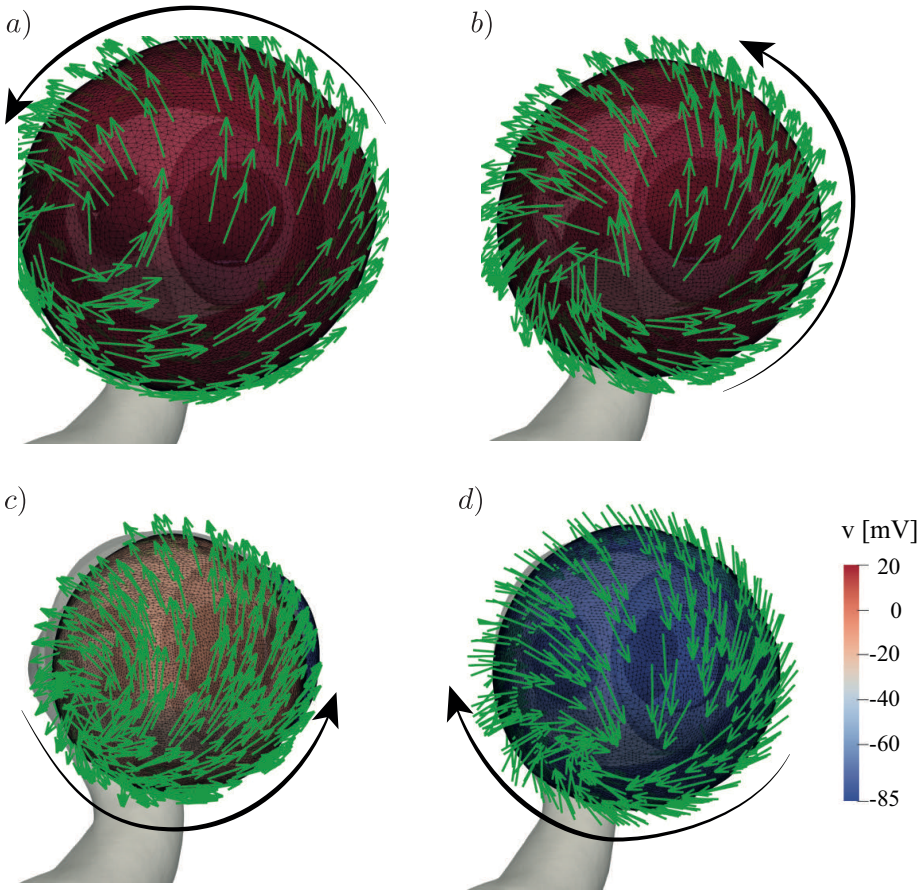


Figure 8: Bottom view of the transmembrane potential propagation in the ventricle during (a-c) contraction and (d) relaxation, which correspond to the time instants $t/T = 0.07, 0.16, 0.3$ and 0.65 in figure 12. The green arrows depict the instantaneous velocity of the material points of the tissue, which reveals the helical motion of the myocardium during systole.

to the root-mean-squares deviation among them. Similarly, figure 9(b) and (c) compare the mean circumferential and longitudinal strain of the ventricle averaged over the myocardium coming from the multi-physics model against in-vivo measurements averaged over the data reported in [76, 77, 78, 79] for (b) and in [80, 81, 82, 83] for (c). During systole the ventricle contraction corresponds to a maximum circumferential and longitudinal strain of about 30% 20% respec-

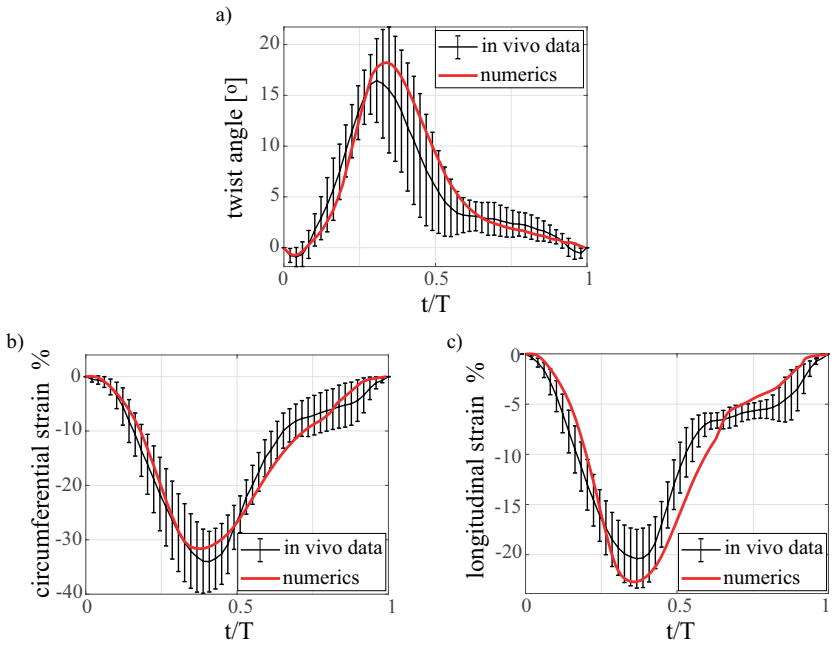


Figure 9: Left ventricle kinematics according to numerics (red line) and in-vivo data (black line): (a) twist angle between apex and basis (b) space–averaged circumferential strain and (c) space–averaged longitudinal strain. The numerical results have been phase averaged over ten heart beats whereas the in-vivo measurements have been obtained by averaging the data from the literature, namely [72, 73, 74, 75] for (a), [76, 77, 78, 79] for (b) and [80, 81, 82, 83] for (c). The error bars indicate the corresponding root-mean-square deviation among the data from the literature.

tively, and an overall agreement can be observed between the in-vivo data and the numerics results, which are generally within the uncertainty range of the experimental results.

3.2. Hemodynamics

The active mechanical contraction of the myocardium and the precise timings of the different chambers causes the blood to move from the atrium to the ventricle and eventually to the aorta; the presence of heart valves assures the correct flow direction with only a negligible backflow that would be detrimental to the pumping efficiency. The resulting LH hemodynamics is reported in fig-

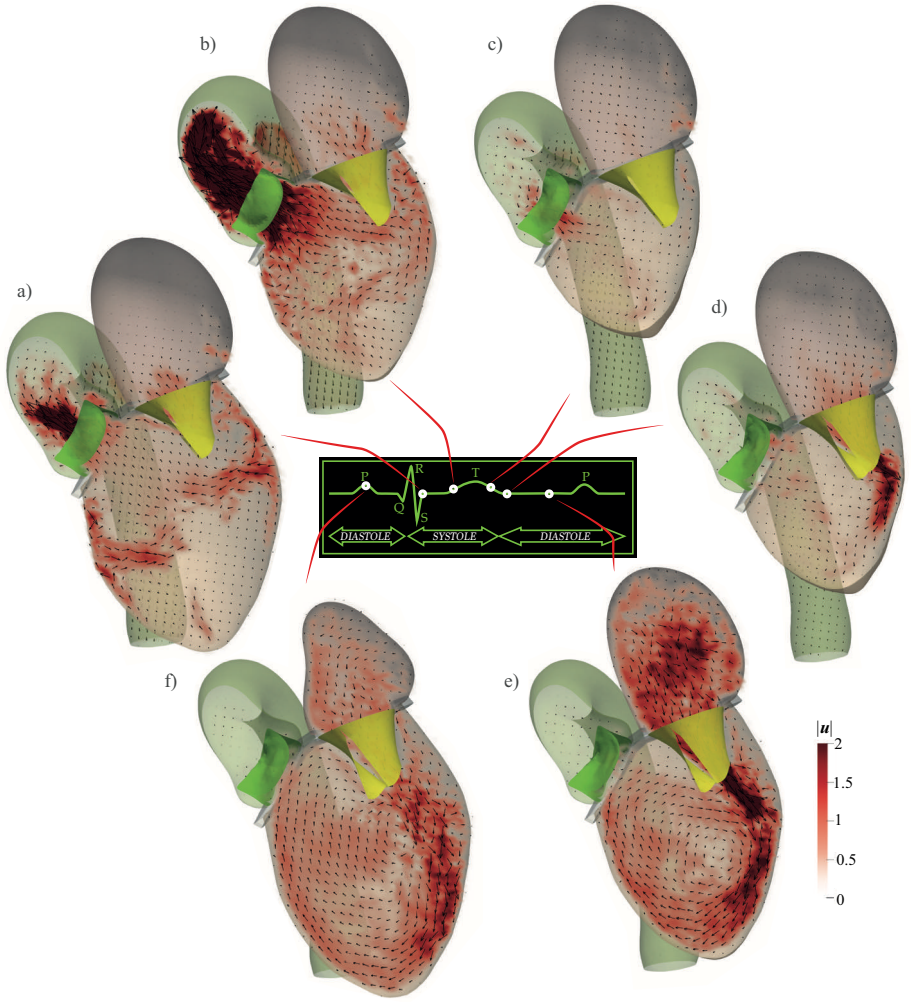


Figure 10: Isocontours of the instantaneous velocity magnitude over a typical ECG signal registered during a heart beat. (a) Early systole, the ventricle contracts and the pressure in the ventricle raises yielding the aortic valve to open (corresponding to the time $t/T = 0.14$ in figure 12); (b) maximum ejection, the aortic valve is fully opened ($t/T = 0.23$); (c) isovolumic relaxation, the aortic valve closes and ventricle stops contracting ($t/T = 0.43$); (d) early diastole, the mitral valve starts opening ($t/T = 0.50$); (e) passive filling during diastole (E-wave, $t/T = 0.6$); (f) atrial systole (A-wave, $t/T = 0.9$).

ures 10 and 11 for representative instants of the heart beat indicated in a typical
680 ECG, where the isocontours of the velocity magnitude and the instantaneous

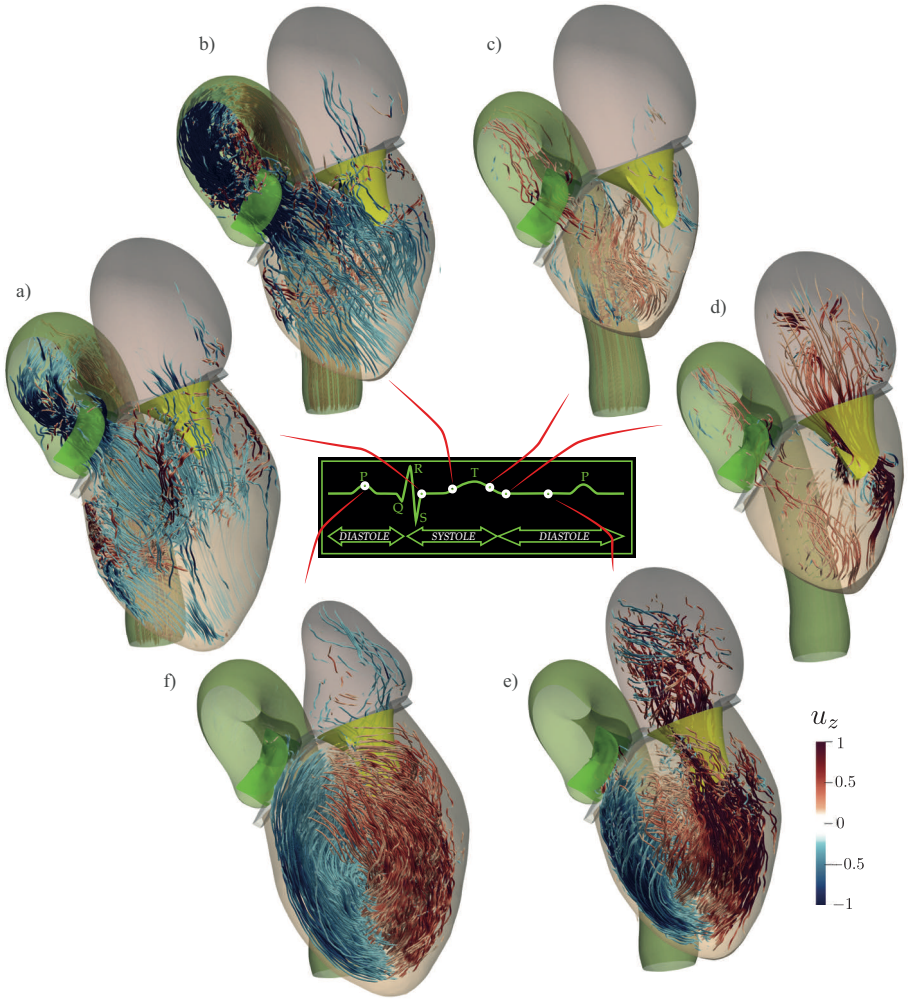


Figure 11: Instantaneous streamlines colored by the vertical velocity over a typical ECG signal registered during a heart beat. The snapshots correspond to the ones in figure 10.

flow streamlines are respectively shown. Keeping in mind that the heart cycle is periodic in time, i.e. every point can be taken as the beginning of the beat, we have arranged the panels of figure 10 and 11 along a circular path to be read in the clockwise direction. For the ease of description, we will start from the QRS–complex of the ECG when the ventricle starts its contraction.

During early systole, owing to the incipient contraction the ventricle, pres-

sure rises and, when it gets larger than that of the aorta (figures 10a and 11a), the aortic valve opens and blood flows to the aorta. As the contraction strengthens the ejected flow rate further increases thus fully opening the tricuspid valve leaflets, until the maximum blood outflow is reached (figures 10b and 11b) and during this phase the maximum blood velocity in the aorta is observed. When the systole ends (figures 10c and 11c), the ventricle volume is minimum (tele–systolic volume) and its myocytes start to repolarize while the active tension decays. Consequently, the pressure in the ventricle drops and aortic valve closes because of the counter pressure between the aorta and the ventricle: the quick aortic valve closure prevents the blood regurgitation in the ventricle that would decrease the pumping efficiency of the heart. As the muscular repolarization progresses, the ventricle relaxes to recover the uncontracted configuration and its increasing volume (figures 10d and 11d) produces a slight under–pressure in the chamber that sucks blood from the atrium and induces the mitral leaflets opening. The blood flow rate from the atrium to the ventricle increases and produces an intense jet (E–wave phase) that does not involve muscular contraction but it is instead driven solely by pressure differences between ventricle and atrium. When the peak flow rate is reached (figures 10e and 11e), the mitral valve opens wider and the jet points vertically downward, reaching the ventricle apex and generating a strong recirculation, which is very beneficial for the hemodynamics since it sweeps the endocardium and prevents the formation of stagnant flow regions [17]. As the passive filling is over, the atrium contracts actively (figures 10f and 11f) and originates a second weaker mitral jet (A–wave) which reinforces the intraventricular recirculation and further expands the ventricle. After atrial systole is complete, the ventricle is ready to receive a new electrical stimulus and the next heart beat can start.

The pressure and volume variations, corresponding to the above described cycle, are shown in figure 12 as a function of time. During the first part of the systole the ventricular pressure increases from the reference (tele-diastolic) value up to the pressure in the thoracic aorta. The ventricular pressure then further increases, yielding the aortic valve open and, as a result, thoracic aorta and

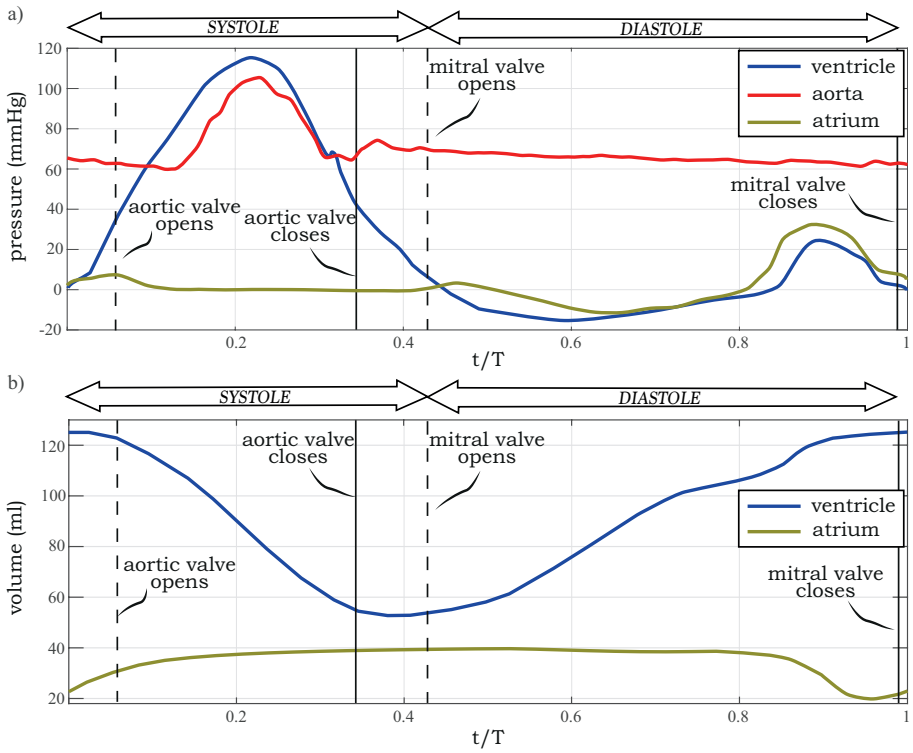


Figure 12: Wiggers diagram [5] resulting from the numerical simulation. The time evolution during a cardiac cycle of phase averaged (a) ventricular, atrial and aortic pressures, along with (b) ventricular and atrial volumes are shown as a function of time normalized by the beating period, t/T.

ventricle become a single chamber, with the two pressure curves following one another quite closely. In this phase the ventricle shrinks, see the volume curve in figure 12(b), and blood is propelled to the systemic circulation while pressure reaches the peak value of about 120 mmHg, which is the highest pressure in the cardiac cycle. The ventricular muscle starts then relaxing and pressure diminishes causing the aortic valve closure at $t/T \sim 0.35$, after which aorta and ventricle become again two separated chambers and the two pressure curves depart. Thereafter, the pressure in the aorta decreases in time very slowly owing to the gradual release of elastic energy, stored in the tension of the tissue, that maintains the blood under a constant pressure while flowing to the

systemic circulation. In contrast, the pressure in the ventricle declines rapidly until the mitral valve opens at $t/T \sim 0.42$ originating a blood inflow from the atrium, which expands the ventricle, as visible in figure 12(b). Ventricular and atrial pressure then exhibit a smaller pressure peak at the end of the diastole ($t/T \simeq 0.9$) that is due to the active atrial systole which shrinks the atrial volume (see figure 12b) and completes the ventricle filling to start a new cycle.

During a heart beat the ventricle's volume diminishes from the maximum (tele–diastolic) volume of $V_{max} = 125$ ml to its minimum (tele–systolic) value of about $V_{min} = 52.79$ ml, corresponding to an ejection fraction of

$$EF = \frac{V_{max} - V_{min}}{V_{max}}\% = 57.77\%, \tag{26}$$

which is a typical physiological value for the heart of a healthy adult. We wish to point out that, while the tele–diastolic volume is given as input through the ventricle geometry, the tele–systolic value is computed as part of the solution therefore the physiologic ejection fraction is one of the consistency checks for the model. Similarly to the ejection fraction of about 60%, also the maximum pressure of 120 mmHg and even the pressure profile during the cycle are all results of the model that are fully consistent with the clinical literature [30] and reproduce both qualitatively and quantitatively the physiological pressure and volume trends for the heart of a healthy adult. Finally when the volumetric output of 12(b) is multiplied by a heart rate of 70 bpm the cardiac output of 5.06 l/min is obtained that again is a physiological value.

The significance of the hemodynamics results is further revealed by monitoring the aortic and mitral flow over a heart cycle. The left panels in figure 13 show the typical (a) aortic outflow and (b) mitral inflow velocity acquired in-vivo through doppler echocardiography, where the sample volume is placed at the aortic and mitral valve tip. The corresponding average velocity coming from numerical simulation is reported in the right panels as a function of time. An overall good agreement between the in-vivo and the numerical results can be observed in terms of velocity profiles. In particular, the ventricle contraction during systole creates the negative velocity peak shown in (a), with a steeper veloc-

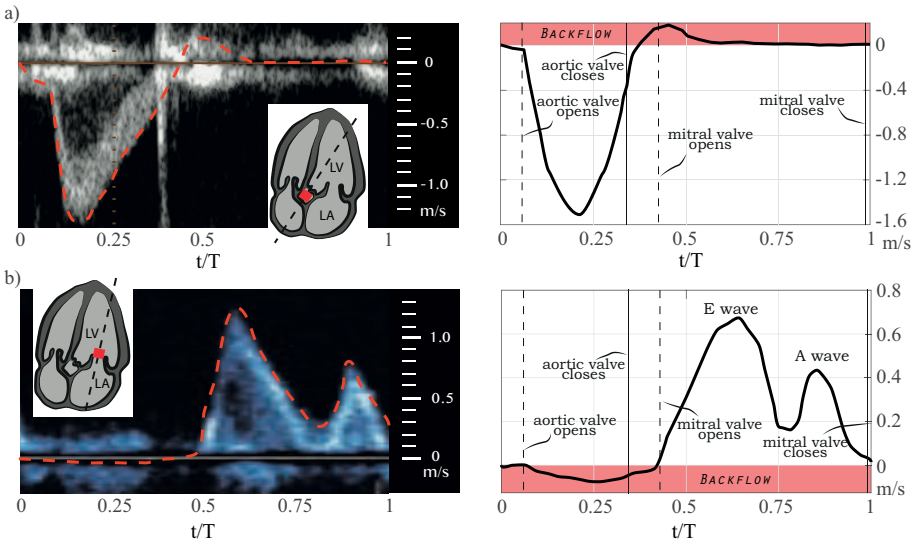


Figure 13: Blood velocity measured in-vivo with Doppler echocardiography (left panels, [36]) and corresponding average velocity from the numerical simulation (right panels) in the (a) aortic and (b) mitral orifices.

ity acceleration ($t/T < 0.23$) and a more gradual flow deceleration ($t/T > 0.23$). During the diastolic phase, the mitral flow presents two velocity peaks, the first corresponding to the early diastole ($t/T = 0.65$, the E–wave) and the second one to the late diastole ($t/T = 0.95$, the A–wave). Note that, despite the velocity peaks are well captured by the in-vivo measurements, the out-of-peak slow velocity are overshadowed by the noise. Conversely, the numerical results are exempt from external noise and the slow inflow and outflow can be promptly measured, thus revealing that a small backflow (of the order of 10% of the peak velocity) manifests after valves closure. It is worth mentioning that this qualitative agreement is satisfactory here since the present model has not been tuned to reproduce exactly the specific patient condition and a one–to-one comparison would only be possible if the exact geometries of the heart chambers, as well as the structural and electrophysiological tissue properties, would be provided as input to the computational model. Furthermore, the peak flow velocity during systole and diastole are very sensitive to the ejection fraction, leaflets geometry

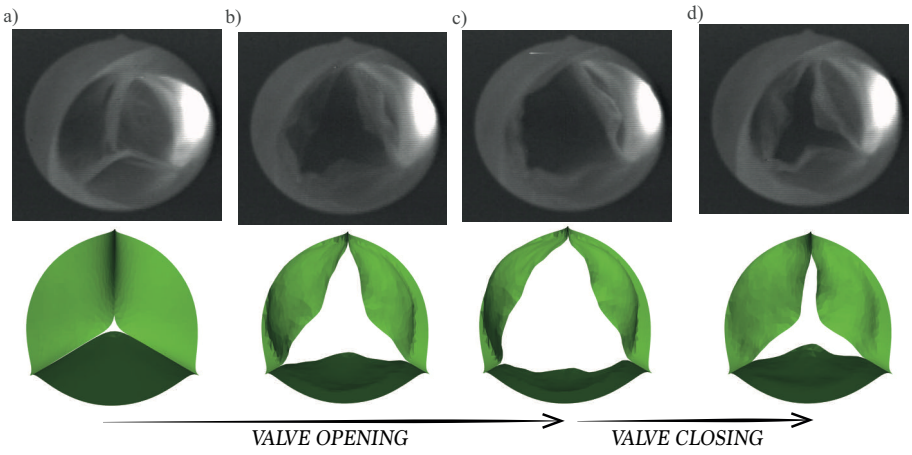


Figure 14: Instantaneous snapshots of the aortic valve leaflets dynamics in (a) closing $t/T = 0.$, (b) partial opening $t/T = 0.1$, (c) full opening $t/T = 0.23$, and (d) partial closing $t/T = 0.3$ configuration. The panels above come from an ex-vivo experiments [84] whereas the ones below are the numerical results.

and valve stenosis [18], but also to the probe positioning and calibration [36].

3.3. Valve dynamics

Let us now focus on the dynamics of the heart valves. Figure 14 shows some representative snapshots of the aortic valve dynamics; the upper panels come from an ex-vivo experiment on a beating pig heart that was arrested, connected to the perfusion system in a laboratory, and restarted using oxygenated balanced saline solution as a working fluid [84]. On the other hand, the lower panels report the corresponding numerical results. Following the previous section, we fix the origin of the cycle at the beginning of the ventricular systole when the aortic valve is closed since the blood pressure in the aorta is bigger than that within the ventricle and the valve leaflets are kept sealed (figure 14a). As the systole progresses the ventricular pressure keeps raising until, when it overcomes the aortic value, the valve starts opening (figure 14b). The valve attains the fully open configuration at the maximum systolic ejection (figure 14c) after which the ventricular pressure drops and the aortic valve starts closing (figure 14d). Once the aortic valve is sealed, it stays closed through the re-

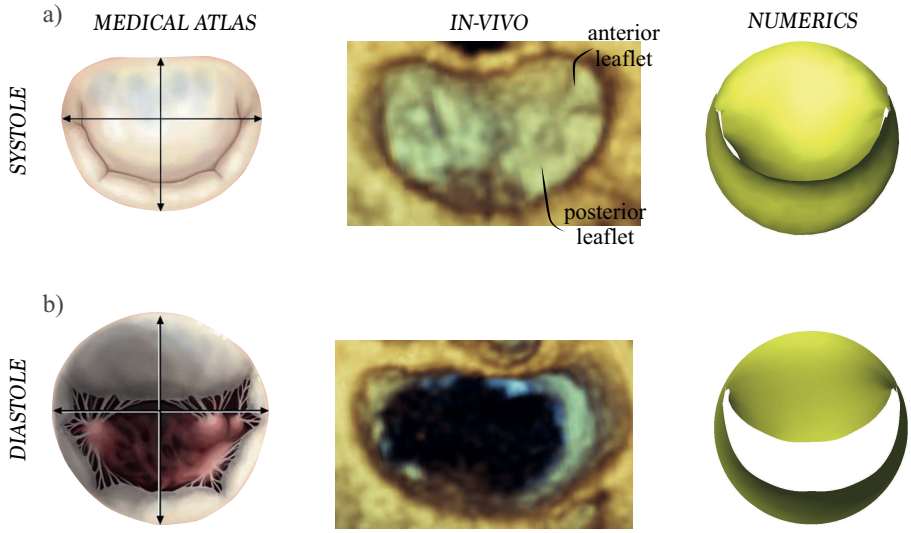


Figure 15: Comparison of (a) closing (peak systole, $t/T = 0.23$) and (b) opening (peak diastole, $t/T = 0.6$) mitral valve configuration between medical atlas [85] (left pictures), in-vivo 3-dimensional transesophageal echocardiography [86] (central pictures) and the computational model (right pictures).

maining part of the cycle until a new ventricular systole occurs and the process repeats. Although the comparison between numerical results and experiments is only qualitative, an overall good agreement in terms of leaflet kinematics and deformations is observed for all phases of the cycle. As discussed in the previous section, this qualitative agreement is satisfactory here since the input parameters of the model have not been calibrated to simulated the specific experiment.

Figure 15 shows the mitral valve configuration fully closed, during ventricular systole and fully open at the peak of the E–wave during diastole. A relatively good agreement is observed between images taken from medical atlas [85] (left panels), in-vivo 3-dimensional transesophageal echocardiography [86] (central pictures) and the valve configuration obtained by the present computational model (right panels). In particular, the typical semilunar shape of the mitral valve orifice during diastole, (figure 15b) and the curved shape of the coaptation

surface (figure 15a), are well reproduced by the model. The latter result is a confirmation that the simple contact model, described in section 2.2, provides realistic leaflet dynamics without prescribing a coaptation surface and it can capture the mitral valve deformation towards the atrium during ventricular systole (figure 15a). Despite the relatively good comparison of figure 15 still there are relevant differences between the model and the biological conditions. One of the most important is the absence deformation of the mitral annulus which is assumed circular, planar and rigid (section 2). In reality the annulus is circular and flat only during diastole (figure 15b) but, when the ventricle contracts, the valvular plane bends to form a saddle and deforms the mitral annulus in an elliptical shape (left panel of figure 15a).

Another important limitation of the present model is the absence of cordae tendineae that link the mitral valve leaflets to the myocardium via the papillary muscles (see for example figure 7a). These cordae prevent the coapted mitral leaflets from everting into the atrium during systole by exerting a tension which pulls the leaflets down into the ventricle. In the present simulations we have prevented the prolapse of the mitral valve by imposing kinematic conditions that limited the vertical displacement of the leaflets during systole. In a separate study [87], however, the present computational model has been already generalized to include the cordae tendineae showing that their main effect is indeed to limit the vertical displacement of the mitral leaflets in the systolic phase.

3.4. Tissue shear stresses

In cardiovascular flows the wall shear stresses (WSS) are an important diagnostic and prognostic quantity since their physiological distribution ensures the functional status of the heart [5, 88] while pathological variations are implied to be responsible of disorders through mechanical hemolysis and tissue remodelling [89, 90]. The complex pulsatile hemodynamics described before entails hydrodynamics loads on the cardiac tissues that are computed by our model as part of the solution. The local WSS magnitude over a surface area oriented as

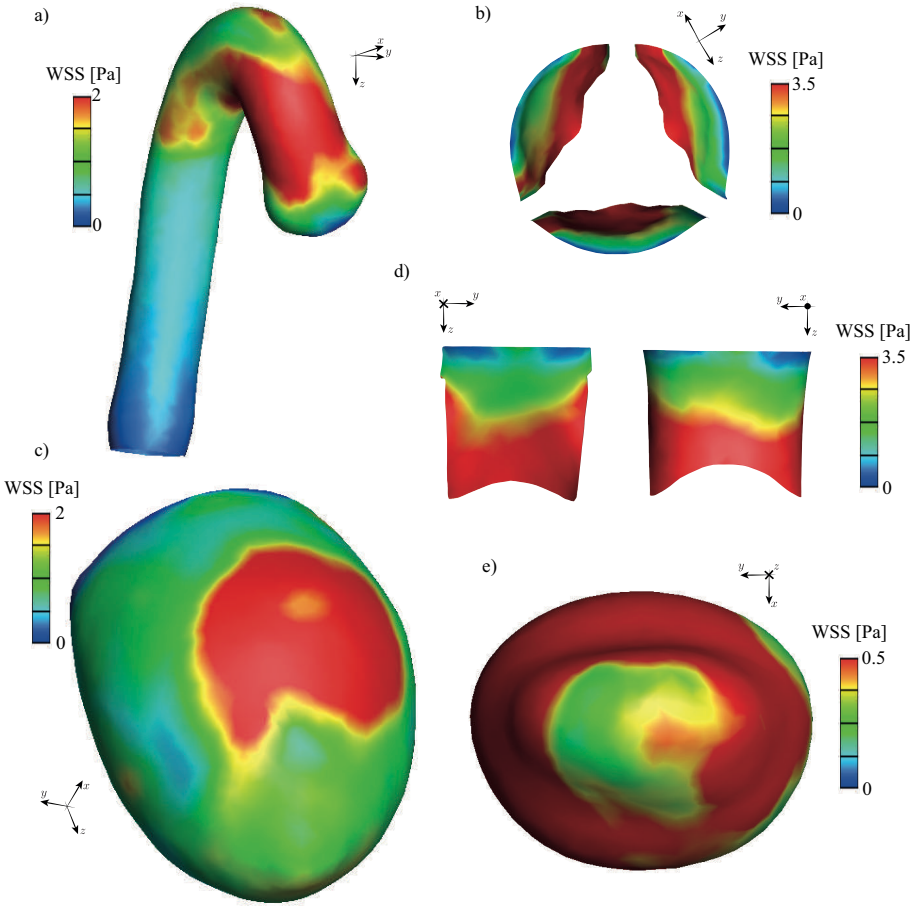


Figure 16: Distribution of the wall shear stresses magnitude in the left heart at peak systole ($t/T = 0.23$) for the (a) aorta and (b) aortic valve; at peak diastole ($t/T = 0.6$) for the (c) ventricle and (d) mitral leaflets; and at the peak atrial systole ($t/T = 0.9$) for (e) the atrium. Quantities have been phase averaged over ten heart beats and the corresponding root-mean-squares are shown in figure 17.

$\mathbf{n}$ can be defined as

$$\text{WSS} = ||\mathbf{t_n} - (\mathbf{t_n} \cdot \mathbf{n})\mathbf{n}||, \tag{27}$$

where $\mathbf{t_n}$ is the stress vector at the wall defined as $\boldsymbol{\tau} \cdot \mathbf{n}$ with $\boldsymbol{\tau}$ the viscous stress tensor defined in section 2.1.

Figure 16 shows the WSS distribution over different regions of the LH at representative instants of the heart beat: for the aorta (a) and the aortic valve

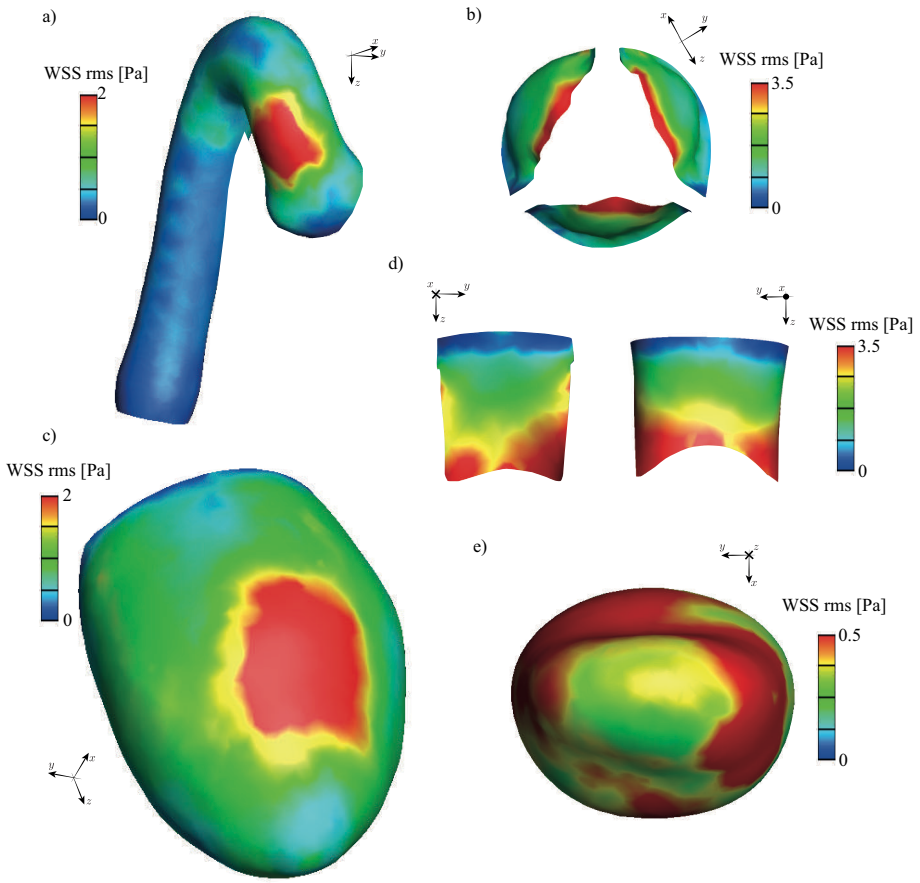


Figure 17: Distribution of the root mean square (rms) of the wall shear stresses magnitude in the left heart. The snapshots correspond to the ones in figure 16.

leaflets (b) the highest values are observed at the peak of the ventricular systole. In contrast, for the ventricle (c) and mitral leaflets (d) the maxima of WSS are achieved at the peak diastole (E–wave). Finally at the peak atrial systole the maxima WSS are obtained for the atrium (e). On each of the surfaces the WSS have a distribution that reflects the instantaneous pattern of the flow sweeping the specific region: in the aorta, the WSS are maxima at the initial ascending tract where the aortic jet, produced by the ventricular contraction, impinges on the inner wall of the vessel. High WSS with an inhomogeneous distribution are also observed in the aortic arch, where the blood flow is bent

	$N_x \times N_y \times N_z$	EF	CO (l/min)
grid 1	$129 \times 129 \times 145$	57.77%	5.06
grid 2	$193 \times 193 \times 257$	59.23%	5.18
grid 3	$257 \times 257 \times 290$	58.10%	5.08

Table 1: Ejection fraction (EF) and cardiac output (CO) dependence on the grid refinement.

rather abruptly into the descending aorta. The WSS are very intense also at the tips of the aortic leaflets where values larger then 3 Pa are measured. Indeed, at the leaflets tip the geometric orifice area is minimum yielding the blood flow to accelerate due to mass conservation. However, since blood velocity has to match the one of the valve leaflets at their surface (no–slip condition), high velocity gradients manifest that correspond to high WSS. The same mechanism holds for the mitral valve during diastole and, consequently, higher WSS are measured at the anterior and posterior leaflets. The highest WSS region in the ventricle is located in the lateral wall where the mitral jet impinges on the myocardium as reported in figure 10(d-f), consistently with previous results [18]. Last, the WSS in the atrium during atrial systole are roughly axisymmetric about its axis with highest values over the lateral walls. The corresponding root-mean-square of the deviation of the instantaneous WSS from the averaged WSS are reported in figure 17. The rms WSS have a similar distribution and magnitude with respect the averaged WSS, which indicate a considerable cycle-to-cycle variation.

These results could be used as reference state to assess the modifications of the WSS distribution produced by any alteration of the either of the geometry or of the functioning parameters; this will be the topic of a future study.

4. Convergence check

In order to assess the numerical convergence of the results, comparative calculations have been carried out for basic (grid 1), fine (grid 2) and very fine (grid 3) grids, as reported in Table 1. Figure 18 shows the ventricular (a) pres-

sure and (b) volume as a function of time, where the curves corresponding to grid 1 were previously reported in the Wiggers diagram [12]. Although some differences are present, a substantial agreement among the results can be observed. In particular, both (a) pressure and (b) volume curves have the same time behaviour with a peak pressure of about 120 mmHg at $t/T = 0.23$ and a tele-systolic volume of about 50 ml. A good agreement is also achieved in terms of clinical relevant parameters such as the ejection fraction (EF) and the cardiac output (CO) with a standard deviation below 2% (see Table 1). It is worthwhile to mention that, despite the fact that the high Reynolds number $Re = 3000$, also the grid 1 provides reasonable accurate results both in terms of pressure and ventricle dynamics with a lower computational cost. Indeed, the Reynolds number is defined at the peak diastolic velocity that lasts only a small fraction of the heart cycle. Additionally, the flow pulsatility yields the flow rate to be small for a significant part of period thus preventing the energy cascade down up to the Kolmogorov scale typical of statistically steady flows.

Figure 19 shows the vertical velocity inside the ventricle at the fixed position $x = 0$, $y = 0$, $z = 1$ phase-averaged over ten cycles for the basic grid 1 and over five cycles for the finest grid 3, where the error bars indicate the the corresponding root-mean-square fluctuations. Although a substantial agreement can be found for the phase-averaged quantities, a considerable cycle-to-cycle variation can be noted due to the dynamics of the small scales, which originate high frequency oscillations. Consequently, the chaotic nature of the flow makes instantaneous comparison of the vertical velocity difficult and local variables are better described using phase-averaged quantities (as done in figure 19), despite the number of integrated heart beats (11 for grid 1 but discarding the first one) is not sufficient to reach statistic convergence of phase-average and rms. This implies that quantitative assessments of the local hemodynamics results can only be obtained by running the model for more heart cycles. In contrast, the instantaneous velocity fluctuations smooth out when the local quantities are space-integrated, as visible in figure 19 where the phase-averaged kinetic energy integrated within the left heart domain for grid 1 and grid 3 well collapse each

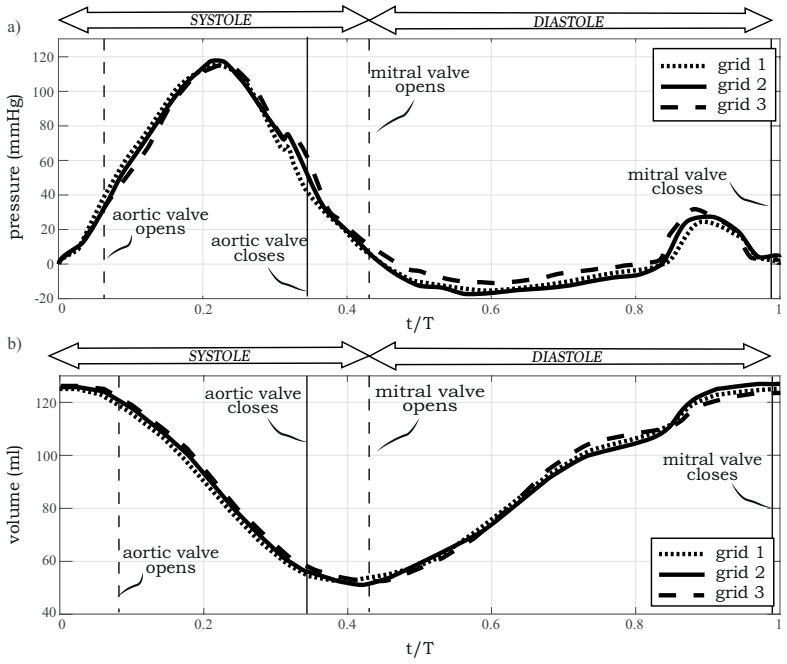


Figure 18: Time evolution during a cardiac cycle of phase–averaged ventricular (a) pressure and (b) volume obtained for the different grids reported in Table 1.

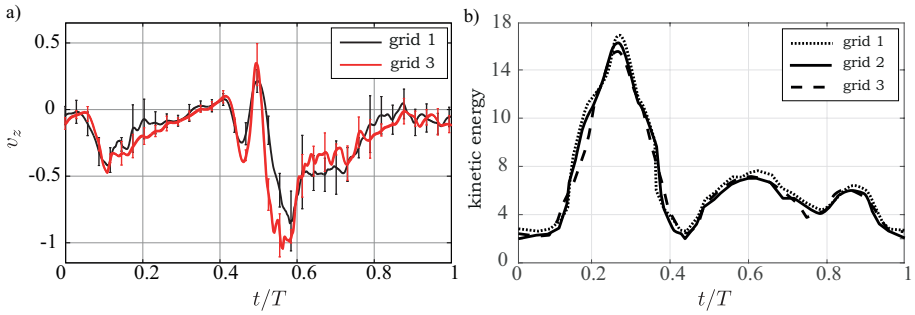


Figure 19: (a) Phase-averaged z-velocity inside the ventricle at the fixed position $x = 0$, $y = 0$, $z = 1$ for grid 1 (black line) and grid 3 (red line). The error bars indicate the corresponding root-mean-squares among the different cycles. b) Phase-averaged kinetic energy integrated within the left heart.

other. These convergence results are in-line with the work of [17] where a mesh equivalent to our grid 1 has been shown to correctly capture ventricle and mitral valve dynamics in the case of a prescribed inflow/outflow in the ventricle, which

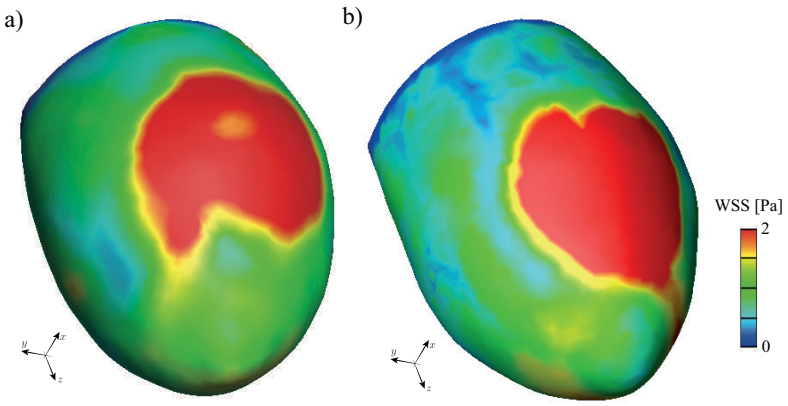


Figure 20: Phase-averaged distribution of the wall shear stresses magnitude in the ventricular endocardium (at peak diastole, $t/T = 0.6$) for (a) grid 1 and (b) grid 3.

has been also validated against dedicated laboratory experiments [17, 44, 91].

Furthermore, figure 20 shows the distribution of the WSS magnitude in the ventricular endocardium (at peak diastole, $t/T = 0.6$) for the basic grid 1 and the more refined grid 3: although some differences are present an overall agreement can be observed.

5. Conclusions

In this work an innovative and versatile multi-physics model to simulate the left heart functioning is proposed. The pulsatile and transitional character of the hemodynamics is obtained by solving directly the incompressible Navier-Stokes equations using a staggered finite differences method. The code is complemented with various immersed boundary (IB) techniques to handle complex moving and deforming geometries. The structural mechanics is based on the Fedosov's interaction potential method [47] to account for the mechanical properties of the biological tissues, which are anisotropic and nonlinear. The electrophysiology, responsible for the active potential propagation in the cardiac tissue triggering the active muscular tension, is incorporated by means of a bidomain model that can account for the different cellular models of the various portions of the

heart. All these models are three–way coupled with each other, thus capturing the fully synergistic physics that allows the heart to function continuously using only 8W of power. The resulting electro-fluid-structure interaction (FSEI) code is tailored to investigate the pulsatile flow in an animated LH beating at 70 bpm. The LH is composed by realistic geometries of the left ventricle and atrium, whose active muscular contraction triggers a structural deformation of the endocardium that originates the hemodynamics, which, in turn, generates stresses on the surrounding cardiac tissue. The numerical framework also includes the bi-leaflet mitral valve, the three-leaflets aortic valve and the thoracic aorta, which are passive tissues experiencing continuous stretching and bending through the cardiac cycle.

The computational framework is seen to provide realistic cardiovascular simulations both in terms of muscular activation, intraventricular hemodynamics and wall shear stresses. In particular, we have shown the propagation of the transmembrane potential over the myocardium triggered by a localized electrical input in the Bachmann and His bundles. The consequent action potential and heart chambers depolarization yields an active muscular tension and tissue contraction that is oriented according to the local direction of the muscular fibers. Hence, the model reproduces also the vigorous three–dimensional twist of the left ventricle from the apex to the valvular plane observed in–vivo [62]. This electro-mechanical activity of the LH chambers originates a complex hemodynamics and valve dynamics, which is in qualitative and quantitative agreement with in-vivo and ex-vivo measurements. The mitral valve connecting the left atrium and ventricle, opens during diastole and closes when the ventricle contracts, owing to the external hydrodynamics loads exerted on its leaflets. At the same time the mitral valve prevents an undesired back–flow of oxygenated blood during systole, the aortic valve opens and blood is propelled in the thoracic aorta. Furthermore, the numerics well reproduces the Wiggers diagram of a healthy human adult reported in medical atlas. This diagram shows the time variation over a heart beat of the pressure in the left ventricle, atrium and thoracic aorta, with the typical pressure variation of $0-120$ mmHg in the ventri-

cle. During a heart beat, the ventricular volume diminishes from the maximum (tele–diastolic) volume, which is given as input through the ventricle geometry, to its minimum (tele–systolic) value, which is not imposed and computed as part of the solution. This volume variation of the ventricle corresponds to an ejection fraction of about 60% and a cardiac output of 5.06 l/min, which are typical physiological values for the heart of a healthy adult.

We wish to stress that the expansion/contraction motion of the heart chambers, along with the heart valves kinematics, results from the combined effect of hydrodynamic loads and internal tissue stresses, which are fully resolved by the FSEI and are not imposed on the basis of empirical data. In kinematics–driven models, indeed, the fluid–structure coupling is only *one–way* meaning that the fluid motion has to adapt to the prescribed tissue displacement and, therefore, physiological cardiac hemodynamics and WSS can be achieved only if the correct structural kinematics is enforced. Hence, in order to study the healthy or pathological cardiac hemodynamics, the instantaneous configuration of all structures for any heart configuration has to be available as input for the numerical solver. In contrast, the body kinematics comes as a result of the three-way FSEI coupling and a different cardiac configuration (e.g. cardiac output, heart rate, ventricle geometry, valve leaflets length and/or thickness) can be simply investigated by minimal modifications in the computational model.

Furthermore, the realistic and detailed blood motion over the moving heart tissues solved by the FSEI also provides the instantaneous hydrodynamic loads acting on the myocardium and valve leaflets, which are overlooked by the electromechanical models where the fluid part is usually neglected or coarsely simplified. The correct solution of the shear stresses (WSS) originated at the wall is of paramount importance for the heart modelling since it is well known that the abnormal WSS distributions activate mechanotransduction mechanisms [92], which in the long term may produce tissue remodelling that eventually leads to the impairing of the organ. Specifically, the cardiac hemodynamics characterized by separation, shedding, recirculations and rich vortex dynamics generate intense WSS at specific locations (see section 3.4), which may alter the phys-

iological stress levels in the surrounding tissues and trigger remodelling. Although the specific models of mechanotransduction are still an area of ongoing research, the endothelial WSS is an important input parameter for these models [93, 94]. Within this scenario, in a future study, the computational heart model introduced here could be used as an initial healthy state to assess the tissue modifications due to remodelling induced by the of the WSS distribution yielding heart pathologies.

The pathological hemodynamics may still be investigated through the FSEI approach. Indeed, thanks to its versatility, the computational model allows to investigate the hemodynamics modification due to cardiac diseases such as in hypertrophic cardiomyopathy. The latter manifests as a thickening of the septal myocardium that obstructs the blood flow into the aorta during systole and can potentially cause heart failure. In this case, the effect of a geometrical modification owing to the hypertrophyc growth on the cardiac output can be studied by starting from a healthy heart, as the one shown here, and progressively increasing the severity of the disease by perturbing the ventricle geometry. Another pathology to be studied is the mitral valve insufficiency in which the mitral valve does not close properly when the heart pumps out blood. In the case of surgical repair, mitral-valve plasty consists in the application of a flexible metal ring whose diameter is typically decided by surgeons based on their own experience. A possible approach would be to combine the information coming from the multi-physics model with the technical tools to predict the patient optimal ring size and how different therapeutic solutions affect the transventricular hemodynamics, the heart pumping efficiency and the hydrodynamic stresses on the biological tissues.

The three-way electro-fluid-structure interaction (FSEI) makes the computational model predictive, thus opening the way to numerical experiments for virtually testing new prosthetic devices and surgical procedures. Nevertheless, the involved multi-physics model also requires many input parameters (elastic properties of the tissue, electrical conductivities, anatomical details), which can vary among different individuals and that can be hardly measured in-vivo,

thus calling for an uncertainty quantification approach. In this framework, the physiological variability among different individuals is accounted by treating the input parameters coming from clinical data as aleatory variables with a variability range provided by their probability distribution (pdf). Hence, several simulations have to be run varying the parameters within their pdf and the hemodynamics results, including the WSS, are in turn aleatory variables with a pdf to be determined.

Acknowledgments

The authors wish to acknowledge M. D. de Tullio for stimulating discussions. F.V. acknowledges the support of the Swiss National Science Foundation (Grant Nos. P2ELP2_172320 and P400P2_180738) and the Marie Curie IF-2017 Program (Grant 792993).

References

[1] S. Mendis, P. Puska, B. Norrving, W. H. Organization, et al., Global atlas on cardiovascular disease prevention and control, Geneva: World Health Organization, 2011.

[2] A. Go, et al., Executive summary: heart disease and stroke statistics2013 update: a report from the american heart association, Circulation 127 (1) (2013) 143–152.

[3] R. Mittal, J. H. Seo, V. Vedula, Y. J. Choi, H. Liu, H. H. Huang, S. Jain, L. Younes, T. Abraham, R. T. George, Computational modeling of cardiac hemodynamics: Current status and future outlook, Journal of Computational Physics 305 (2016) 1065–1082.

[4] R. Mittal, Matters of the heart, Journal of Fluid Mechanics 844 (2018) 1–4.

[5] J. E. Hall, Guyton and Hall textbook of medical physiology, Elsevier Health Sciences, 2010.

[6] M. Jahangiri, M. Saghafian, M. R. Sadeghi, Numerical study of turbulent pulsatile blood flow through stenosed artery using fluid-solid interaction, Computational and mathematical methods in medicine 2015.

[7] J. Lantz, J. Renner, M. Karlsson, Wall shear stress in a subject specific human aortainfluence of fluid-structure interaction, International Journal of Applied Mechanics 3 (04) (2011) 759–778.

[8] M. R. Myers, J. M. Porter, Impulsive-motion model for computing the closing motion of mechanical heart-valve leaflets, Annals of biomedical engineering 31 (9) (2003) 1031–1039.

[9] Y. Cheng, H. Oertel, T. S., Fluid-structure coupled cfd simulation of the left ventricular flow during filling phase, Annals of biomedical engineering 33 (5) (2005) 567–576.

[10] I. Borazjani, L. Ge, L. P. Sotiropoulos, F.and Dasi, A. Yogonathan, Fluid-structure interaction in bi-leaflet mechanical heart valves, in: ASME 2007 2nd Frontiers in Biomedical Devices Conference, American Society of Mechanical Engineers, 2007, pp. 17–18.

[11] M. D. De Tullio, A. Cristallo, E. Balaras, R. Verzicco, Direct numerical simulation of the pulsatile flow through an aortic bileaflet mechanical heart valve, Journal of Fluid Mechanics 622 (2009) 259–290.

[12] M. Grigioni, U. Morbiducci, G. D'Avenio, G. Di Benedetto, C. Del Gaudio, A novel formulation for blood trauma prediction by a modified power-law mathematical model, Biomechanics and Modeling in Mechanobiology 4 (4) (2005) 249–260.

[13] Y. Alemu, D. Bluestein, Flow-induced platelet activation and damage accumulation in a mechanical heart valve: numerical studies, Artificial organs 31 (9) (2007) 677–688.

[14] M. D. De Tullio, G. Pascazio, L. Weltert, R. De Paulis, R. Verzicco, Evaluation of prosthetic-valved devices by means of numerical simulations, Philo-

sophical Transactions of the Royal Society of London A: Mathematical, Physical and Engineering Sciences 369 (1945) (2011) 2502–2509.

[15] M. D. De Tullio, L. Afferrante, G. Demelio, G. Pascazio, R. Verzicco, Fluid-structure interaction of deformable aortic prostheses with a bileaflet mechanical valve, Journal of biomechanics 44 (9) (2011) 1684–1690.

[16] R. Verzicco, Cardiovascular fluid dynamics, in: 7th summer school Complex Motion in Fluids, 2016.

[17] V. Meschini, M. De Tullio, G. Querzoli, R. Verzicco, Flow structure in healthy and pathological left ventricles with natural and prosthetic mitral valves, Journal of fluid mechanics 834 (2018) 271–307.

[18] V. Meschini, F. Viola, R. Verzicco, Modeling mitral valve stenosis: A parametric study on the stenosis severity level, Journal of biomechanics.

[19] T. Schenkel, M. Malve, M. Reik, M. Markl, B. Jung, H. Oertel, Mri-based cfd analysis of flow in a human left ventricle: methodology and application to a healthy heart, Annals of biomedical engineering 37 (3) (2009) 503–515.

[20] L. Tung, A bi-domain model for describing ischemic myocardial dc potentials., Ph.D. thesis, Massachusetts Institute of Technology (1978).

[21] R. H. Clayton, A. V. Panfilov, A guide to modelling cardiac electrical activity in anatomically detailed ventricles, Progress in biophysics and molecular biology 96 (1) (2008) 19–43.

[22] D. M. Roden, J. R. Balser, G. J. A. L., M. E. Anderson, Cardiac ion channels, Annual review of physiology 64 (1) (2002) 431–475.

[23] M. Fink, S. A. Niederer, E. M. Cherry, F. H. Fenton, J. T. Koivumäki, G. Seemann, R. Thul, H. Zhang, F. B. Sachse, D. Beard, E. Crampin, N. P. Smith, Cardiac cell modelling: observations from the heart of the cardiac physiome project, Progress in biophysics and molecular biology 104 (1) (2011) 2–21.

[24] J. Cooper, A. Corrias, D. Gavaghan, D. Noble, Considerations for the use of cellular electrophysiology models within cardiac tissue simulations, Progress in biophysics and molecular biology 107 (1) (2011) 74–80.

[25] P. Pathmanathan, M. O. Bernabeu, R. Bordas, J. Cooper, A. Garny, J. M. Pitt-Francis, J. P. Whiteley, D. J. Gavaghan, A numerical guide to the solution of the bidomain equations of cardiac electrophysiology, Progress in biophysics and molecular biology 102 (2) (2010) 136–155.

[26] S. A. Niederer, E. Kerfoot, A. P. Benson, M. O. Bernabeu, O. Bernus, C. Bradley, E. M. Cherry, R. Clayton, F. H. Fenton, A. Garny, E. Heidenreich, S. Land, M. Maleckar, P. Pathmanathan, G. Plank, I. Rodrguez, J. F. abd Roy, F. B. Sachse, G. Seemann, O. Skavhaug, N. P. Smith, Verification of cardiac tissue electrophysiology simulators using an n-version benchmark, Phil. Trans. R. Soc. A 369 (1954) (2011) 4331–4351.

[27] H. Watanabe, S. Sugiura, H. Kafuku, T. Hisada, Multiphysics simulation of left ventricular filling dynamics using fluid-structure interaction finite element method, Biophysical journal 87 (3) (2004) 2074–2085.

[28] E. J. Vigmond, C. Clements, D. M. McQueen, C. S. Peskin, Effect of bundle branch block on cardiac output: a whole heart simulation study, Progress in biophysics and molecular biology 97 (2) (2008) 520–542.

[29] T. B. Le, F. Sotiropoulos, Fluid-structure interaction of an aortic heart valve prosthesis driven by an animated anatomic left ventricle, Journal of computational physics 244 (2013) 41–62.

[30] G. Stouffer, M. S. Runge, C. Patterson, J. S. Rossi, Netter's Cardiology, Elsevier Health Sciences, 2018.

[31] M. D. De Tullio, Pascazio, A moving-least-squares immersed boundary method for simulating the fluid-structure interaction of elastic bodies with arbitrary thickness, to appear in Journal of Computational Physics.

[32] F. De Vita, M. D. de Tullio, R. Verzicco, Numerical simulation of the non-newtonian blood flow through a mechanical aortic valve, Theoretical and Computational Fluid Dynamics 30(1) (2016) 129–138.

[33] D. A. Siginer, D. De Kee, R. P. Chhabra, Advances in the flow and Rheology of non-Newtonian fluids, Elsevier, Amsterdam, 1999.

[34] D. Katritsis, L. Kaiktsis, A. Chaniotis, J. Pantos, E. P. Efstathopoulos, V. Marmarelis, Wall shear stress: theoretical considerations and methods of measurement, Progress in cardiovascular diseases 49 (5) (2007) 307–329.

[35] F. De Vita, M. D. de Tullio, R. Verzicco, Numerical simulation of the blood flow in the aortic root with a non-newtonian fluid model, in: AIMETA Conference, 2013, pp. 1–8.

[36] B. Bulwer, J. Rivero, Echocardiography pocket guide: the transthoracic examination, Jones & Bartlett Learning, 2010.

[37] Afid, www.afid.eu.

[38] E. P. van der Poel, R. Ostilla-Mónico, J. Donners, R. Verzicco, A pencil distributed finite difference code for strongly turbulent wall-bounded flows, Computers & Fluids 116 (2015) 10–16.

[39] M. Rai, P. Moin, Direct simulations of turbulent flow using finite-difference schemes, in: 27th Aerospace Sciences Meeting, 1991, p. 369.

[40] R. Verzicco, P. Orlandi, A finite-difference scheme for three-dimensional incompressible flows in cylindrical coordinates, Journal of Computational Physics 123 (2) (1996) 402–414.

[41] E. Fadlun, R. Verzicco, P. Orlandi, J. Mohd-Yusof, Combined immersed-boundary finite-difference methods for three-dimensional complex flow simulations, Journal of computational physics 161 (1) (2000) 35–60.

[42] M. Vanella, E. Balaras, A moving–least–squares reconstruction for embedded–boundary formulations, Journal of Computational Physics 228(18) (2009) 6617–6628.

[43] M. Uhlmann, An immersed boundary method with direct forcing for the simulation of particulate flows, Journal of Computational Physics 209 (2) (2005) 448–476.

[44] V. Spandan, V. Meschini, R. Ostilla-Mónico, D. Lohse, G. Querzoli, M. D. de Tullio, R. Verzicco, A parallel interaction potential approach coupled with the immersed boundary method for fully resolved simulations of deformable interfaces and membranes, Journal of computational physics 348 (2017) 567–590.

[45] V. Spandan, D. Lohse, M. D. de Tullio, R. Verzicco, A fast moving least squares approximation with adaptive lagrangian mesh refinement for large scale immersed boundary simulations, Journal of computational physics 375 (2018) 228–239.

[46] M. Beeson, Triangle tiling i: the tile is similar to abc or has a right angle, arXiv preprint arXiv:1206.2231.

[47] D. A. Fedosov, B. Caswell, G. E. Karniadakis, Systematic coarse-graining of spectrin-level red blood cell models, Computer Methods in Applied Mechanics and Engineering 199 (29-32) (2010) 1937–1948.

[48] V. Spandan, V. Meschini, R. Ostilla-Mónico, D. Lohse, G. Querzoli, M. D. de Tullio, R. Verzicco, A parallel interaction potential approach coupled with the immersed boundary method for fully resolved simulations of deformable interfaces and membranes, Journal of computational physics 348 (2017) 567–590.

[49] A. V. Gelder, Approximate simulation of elastic membranes by triangulated spring meshes, Journal of graphics tools 3 (2) (1998) 21–41.

[50] P. E. Hammer, M. S. Sacks, J. Pedro, R. D. Howe, Mass-spring model for simulation of heart valve tissue mechanical behavior, Annals of biomedical engineering 39 (6) (2011) 1668–1679.

[51] F. C. Yin, R. K. Strumpf, P. H. Chew, S. L. Zeger, Quantification of the mechanical properties of noncontracting canine myocardium under simultaneous biaxial loading, Journal of biomechanics 20 (6) (1987) 577–589.

[52] T. Usyk, R. Mazhari, A. McCulloch, Effect of laminar orthotropic myofiber architecture on regional stress and strain in the canine left ventricle, Journal of elasticity and the physical science of solids 61 (1-3) (2000) 143–164.

[53] G. A. Holzapfel, Determination of material models for arterial walls from uniaxial extension tests and histological structure, Journal of theoretical biology 238 (2) (2006) 290–302.

[54] H. Taghizadeh, M. Tafazzoli-Shadpour, M. Shadmehr, N. Fatouraee, Evaluation of biaxial mechanical properties of aortic media based on the lamellar microstructure, Materials 8 (1) (2015) 302–316.

[55] P. E. Hammer, M. S. Sacks, J. Pedro, R. D. Howe, Mass-spring model for simulation of heart valve tissue mechanical behavior, Annals of biomedical engineering 39 (6) (2011) 1668–1679.

[56] K. May-Newman, F. Yin, A constitutive law for mitral valve tissue, Journal of biomechanical engineering 120 (1) (1998) 38–47.

[57] J. F. Wenk, M. B. Ratcliffe, J. M. Guccione, Finite element modeling of mitral leaflet tissue using a layered shell approximation, Medical & biological engineering & computing 50 (10) (2012) 1071–1079.

[58] A. Satriano, C. Bellini, E. J. Vigmond, E. S. Di Martino, A feature-based morphing methodology for computationally modeled biological structures applied to left atrial fiber directions, Journal of biomechanical engineering 135 (3) (2013) 031001.

[59] A. Satriano, E. J. Vigmond, D. S. Schwartzman, E. S. Di Martino, Mechano-electric finite element model of the left atrium, Computers in biology and medicine 96 (2018) 24–31.

[60] Y. Kantor, D. R. Nelson, Phase transitions in flexible polymeric surfaces, Physical Review A 36 (8) (1987) 4020.

[61] J. Li, M. Dao, C. Lim, S. Suresh, Spectrin-level modeling of the cytoskeleton and optical tweezers stretching of the erythrocyte, Biophysical journal 88 (5) (2005) 3707–3719.

[62] F. Torrent-Guasp, M. J. Kocica, A. Corno, M. Komeda, J. Cox, A. Flotats, M. Ballester-Rodes, F. Carreras-Costa, Systolic ventricular filling, European journal of cardio-thoracic surgery 25 (3) (2004) 376–386.

[63] J. Sundnes, G. T. Lines, X. Cai, B. F. Nielsen, K.-A. Mardal, A. Tveito, Computing the electrical activity in the heart, Vol. 1, Springer Science & Business Media, 2007.

[64] K. Ten Tusscher, A. Panfilov, Cell model for efficient simulation of wave propagation in human ventricular tissue under normal and pathological conditions, Physics in Medicine & Biology 51 (23) (2006) 6141.

[65] R. Fitzhugh, Thresholds and plateaus in the hodgkin-huxley nerve equations, The Journal of general physiology 43 (5) (1960) 867–896.

[66] M. S. Alnæs, J. Blechta, J. Hake, A. Johansson, B. Kehlet, A. Logg, C. Richardson, J. Ring, M. E. Rognes, G. N. Wells, The fenics project version 1.5, Archive of Numerical Software 3 (100).

[67] A. Logg, K.-A. Mardal, G. N. Wells, et al., Automated Solution of Differential Equations by the Finite Element Method, Springer, 2012.

[68] M. E Rognes, P. E Farrell, S. W Funke, J. E Hake, M. MC Maleckar, cbcbeat: an adjoint-enabled framework for computational cardiac electrophysiology, The Journal of Open Source Software 2.

[69] M. P. Nash, A. V. Panfilov, Electromechanical model of excitable tissue to study reentrant cardiac arrhythmias, Progress in biophysics and molecular biology 85 (2-3) (2004) 501–522.

[70] S. Göktepe, E. Kuhl, Electromechanics of the heart: a unified approach to the strongly coupled excitation–contraction problem, Computational Mechanics 45 (2-3) (2010) 227–243.

[71] R. Clayton, O. Bernus, E. Cherry, H. Dierckx, F. Fenton, L. Mirabella, A. V. Panfilov, F. B. Sachse, G. Seemann, H. Zhang, Models of cardiac tissue electrophysiology: progress, challenges and open questions, Progress in biophysics and molecular biology 104 (1) (2011) 22–48.

[72] G. Buckberg, A. Mahajan, S. Saleh, J. I. Hoffman, C. Coghlan, Structure and function relationships of the helical ventricular myocardial band, The Journal of thoracic and cardiovascular surgery 136 (3) (2008) 578–589.

[73] E. J. Stöhr, R. E. Shave, A. L. Baggish, R. B. Weiner, Left ventricular twist mechanics in the context of normal physiology and cardiovascular disease: a review of studies using speckle tracking echocardiography, American Journal of Physiology-Heart and Circulatory Physiology 311 (3) (2016) H633–H644.

[74] A. M. S. Omar, S. Vallabhajosyula, P. P. Sengupta, Left ventricular twist and torsion: research observations and clinical applications, Circulation: Cardiovascular Imaging 8 (6) (2015) e003029.

[75] P. P. Sengupta, A. J. Tajik, K. Chandrasekaran, B. K. Khandheria, Twist mechanics of the left ventricle: principles and application, JACC: Cardiovascular Imaging 1 (3) (2008) 366–376.

[76] D. Auger, M. J. Schalij, J. J. Bax, V. Delgado, Three-dimensional imaging in cardiac resynchronization therapy, Revista Española de Cardiología (English Edition) 64 (11) (2011) 1035–1044.

[77] J. Huang, Z.-N. Yan, Y.-F. Rui, L. Fan, C. Liu, J. Li, Left ventricular short-axis systolic function changes in patients with hypertrophic cardiomyopathy detected by two-dimensional speckle tracking imaging, BMC cardiovascular disorders 18 (1) (2018) 13.

[78] R. J. Taylor, W. E. Moody, F. Umar, N. C. Edwards, T. J. Taylor, B. Stegemann, J. N. Townend, K. N. Hor, R. P. Steeds, W. Mazur, et al., Myocardial strain measurement with feature-tracking cardiovascular magnetic resonance: normal values, European Heart Journal–Cardiovascular Imaging 16 (8) (2015) 871–881.

[79] J. Chan, L. Hanekom, C. Wong, R. Leano, G.-Y. Cho, T. H. Marwick, Differentiation of subendocardial and transmural infarction using two-dimensional strain rate imaging to assess short-axis and long-axis myocardial function, Journal of the American College of Cardiology 48 (10) (2006) 2026–2033.

[80] O. A. Smiseth, H. Torp, A. Opdahl, K. H. Haugaa, S. Urheim, Myocardial strain imaging: how useful is it in clinical decision making?, European heart journal 37 (15) (2015) 1196–1207.

[81] A. D'Andrea, E. Bossone, J. Radmilovic, P. Caso, R. Calabrò, M. G. Russo, M. Galderisi, The role of new echocardiographic techniques in athlete's heart, F1000Research 4.

[82] K. Addetia, M. Takeuchi, F. Maffessanti, Y. Nagata, J. Hamilton, V. Mor-Avi, R. M. Lang, Simultaneous longitudinal strain in all 4 cardiac chambers: a novel method for comprehensive functional assessment of the heart, Circulation: Cardiovascular Imaging 9 (3) (2016) e003895.

[83] A. Singh, K. Addetia, F. Maffessanti, V. Mor-Avi, R. M. Lang, La strain for categorization of lv diastolic dysfunction, JACC: Cardiovascular Imaging 10 (7) (2017) 735–743.

[84] Valveguru, Wikimedia Commons CC BY-SA 3.0 299 (1989) 134–143.

[85] A. Carpentier, D. H. Adams, F. Filsoufi, Carpentier's Reconstructive Valve Surgery E-Book, Elsevier Health Sciences, 2011.

[86] Y. Rim, S. T. Laing, P. Kee, D. D. McPherson, H. Kim, Evaluation of mitral valve dynamics, JACC: Cardiovascular Imaging 6 (2) (2013) 263–268.

[87] V. Meschini, M. De Tullio, R. Verzicco, Effects of mitral chordae tendineae on the flow in the left heart ventricle, European Physical Journal E, Soft Matter 41 (2018) 27.

[88] E. Picano, E. Picano, Stress echocardiography, Springer, 2003.

[89] D. G. Guzzardi, A. J. Barker, P. Van Ooij, S. C. Malaisrie, J. J. Puthumana, D. D. Belke, H. E. Mewhort, D. A. Svystonyuk, S. Kang, S. Verma, et al., Valve-related hemodynamics mediate human bicuspid aortopathy: insights from wall shear stress mapping, Journal of the American College of Cardiology 66 (8) (2015) 892–900.

[90] J. T. Butcher, R. M. Nerem, Valvular endothelial cells regulate the phenotype of interstitial cells in co-culture: effects of steady shear stress, Tissue engineering 12 (4) (2006) 905–915.

[91] F. Viola, E. Jermyn, J. Warnock, G. Querzoli, R. Verzicco, Left ventricular hemodynamics with an implanted assist device: An in vitro fluid dynamics study, Annals of biomedical engineering (2019) 1–16.

[92] V. Y. Wang, J. R. Hussan, H. Yousefi, C. P. Bradley, P. J. Hunter, M. P. Nash, Modelling cardiac tissue growth and remodelling, Journal of Elasticity 129 (1-2) (2017) 283–305.

[93] M. L. Kutys, C. S. Chen, Forces and mechanotransduction in 3d vascular biology, Current opinion in cell biology 42 (2016) 73–79.

[94] B. D. Johnson, K. J. Mather, J. P. Wallace, Mechanotransduction of shear in the endothelium: basic studies and clinical implications, Vascular medicine 16 (5) (2011) 365–377.